# Tonian carbonates record phosphate-rich shallow seas

**Sascha Roest-Ellis[1], Jocelyn A. Richardson[2], Brian L. Phillips[3], Akshay Mehra[4*], Samuel M. Webb[2], Phoebe A. Cohen[5], Justin V. Strauss[4], Nicholas J. Tosca[6]**

[1]Department of Earth Sciences, University of Oxford, Oxford, OX1 3AN, UK
[2]SLAC National Accelerator Laboratory, Stanford Synchrotron Radiation Lightsource, Menlo Park, CA 94025, USA
[3]Department of Geosciences, Stony Brook University, Stony Brook, NY 11794, USA
[4]Department of Earth Sciences, Dartmouth College, Hanover, NH 03755, USA
[5]Department of Geosciences, Williams College, Williamstown, MA 01267, USA
[6]Department of Earth Sciences, University of Cambridge, Cambridge, CB2 3EQ, UK

**Key Points:**

- NMR, XANES, and $\mu$-XRF reveal distribution and speciation of P in Tonian shallow-water carbonates
- New microanalytical data and geochemical constraints indicate higher shallow water phosphate concentrations than modern systems
- Kinetic controls on $CaCO_3$ deposition, mediated by P, may have destabilised marine carbonate chemistry, climate, and nutrient inventories

*Current address: Department of Earth and Space Sciences, University of Washington, Seattle, WA 98195, USA

Corresponding author: Nicholas J. Tosca, njt41@cam.ac.uk

**Abstract**

The early-middle Neoproterozoic is thought to have witnessed significant perturbations to marine P cycling, in turn facilitating the rise of eukaryote-dominated primary production. However, with few robust constraints on aqueous P concentrations, current understanding of Neoproterozoic P cycling is generally model-dependent. To provide new geochemical constraints, we combined microanalytical datasets with solid-state NMR, synchrotron-based XANES spectroscopy, and micro-XRF imaging to characterise the speciation and distribution of P in Tonian shallow-water carbonate rocks. These data reflect shallow water phosphate concentrations 10-100x higher than modern systems, supporting the hypothesis that tectonically-driven influxes in P periodically initiated kinetically-controlled $CaCO_3$ deposition, in turn destabilising marine carbonate chemistry, climate, and nutrient inventories. Alongside these observations, a new compilation and statistical analysis of mudstone geochemistry data indicates that, in parallel, $C_{org}$ and P burial increased across later Tonian continental margins until becoming decoupled at the close of the Tonian, implicating widespread N-limitation triggered by increasing atmospheric $O_2$.

## Plain Language Summary

As an essential nutrient for all life on Earth, changes in the availability of seawater phosphate over geological timescales are thought to have regulated biospheric productivity and ecosystem structure. Increases in marine phosphate availability in the Neoproterozoic Era (1000 to 538 million years ago), inferred from the total concentration of P in mudstones, are thought to have driven the emergence of eukaryotic algae. However, the causes are not well understood because the concentration of P in mudstones is difficult to relate to seawater phosphate concentrations. To address this problem, we applied new analytical methods to probe the distribution and mineral hosts of phosphate in shallow water carbonate rocks, which permits new estimates for ancient seawater phosphate concentrations. These results reflect shallow water phosphate concentrations several times higher than the modern ocean. Elevated phosphate may have strongly impacted the rate and tempo of carbonate mineral production from Neoproterozoic seas, consistent with geological evidence. This may have driven fluctuations in seawater carbonate chemistry and climate, impacting other critical nutrients such as dissolved inorganic nitrogen. These fluctuations may have presented ancient eukaryotic algae with challenges and opportunities, but their causality and timing remain unclear.

## 1 Introduction

The Neoproterozoic Era (1000 to 538 Ma) witnessed significant shifts in the intensity of physical and chemical weathering (G. M. Cox et al., 2016; Hoffman et al., 2017), atmospheric $pCO_2$ and climate (Pierrehumbert et al., 2011; Hoffman et al., 2017), and the redox state of marine systems (Sperling et al., 2015; Stolper & Keller, 2018; Stolper & Bucholz, 2019). Across this same interval, Neoproterozoic sedimentary rocks archive the emergence of eukaryote-dominated primary production (Brocks et al., 2017), and ultimately the diversification of early animal life (Erwin et al., 2012). Because the supply of P to the marine biosphere is generally assumed to have limited primary productivity over geological timescales (Tyrrell, 1999), in turn modulating organic carbon burial and the accumulation of atmospheric oxygen (VanCappellen & Ingall, 1996; Laakso & Schrag, 2014), constraining the size and dynamics of the Neoproterozoic P reservoir lies at the heart of understanding Earth system change through a critical interval in the history of life.

In the absence of direct constraints on aqueous P concentrations, current models of Neoproterozoic phosphorus cycling have been derived almost exclusively from the bulk concentration of P in fine-grained sedimentary rocks. However, these data have proven difficult to interpret; without additional constraints on the origins and diagenetic histories of P mineral hosts, sedimentary P abundances cannot easily be linked to aqueous P concentrations

or to the size of the marine bioavailable P reservoir (Poulton, 2017). In addition, because water column P concentrations are typically modulated by redox-dependent recycling of P released from sediments (Ingall & Jahnke, 1994; VanCappellen & Ingall, 1994; Poulton, 2017), inferences made from the sedimentary P record commonly rely on interpretations of depositional and diagenetic redox conditions. For example, Reinhard et al. (2017) showed that the average P concentration of Proterozoic shales remained relatively low until the Cryogenian Period (720 to ca. 635 Ma), and interpreted these changes to reflect the demise of a deep-marine P sink mediated by ferrous iron ($Fe^{2+}$; Laakso & Schrag, 2014; Derry, 2015). Employing a similar database, Laakso et al. (2020) argued that although individual occurrences of P-rich sediments (i.e., phosphorites) increase across the later Neoproterozoic, shale-hosted P concentrations do not change across this interval. Laakso et al. (2020) showed that significant changes to the deep-water aqueous phosphate reservoir could have instead been driven by increases in Ediacaran (635 to 541 Ma) marine sulfate concentrations, which in turn facilitated increased organic matter remineralisation and deep water P-regeneration. A more recent analysis of an expanded database suggests that the P concentration of shales began to increase earlier than previously thought (ca. 750 Ma; Planavsky et al., 2022). Utilising a different approach, Guilbaud et al. (2020) used the operationally-defined leaching behaviour of P bound in sedimentary rocks to infer that the low average P concentrations of these shales reflect phosphate-limited primary production from ca. 1000-900 Ma. While these collective results suggest perturbations to the sedimentary P reservoir may have occurred during the Tonian Period (1000 to ca. 720 Ma), potential transitions in P cycling across this interval are not well constrained and are generally model-dependent.

Independently, however, early-middle Neoproterozoic carbonate rocks host microfossil evidence for multiple occurrences of apatite biomineralization across several Tonian basins (Cohen et al., 2017; Moczydłowska et al., 2018; Riedman et al., 2021). These microfossils, which record complex, template-controlled crystallisation of apatite preserved at the nanometer scale (Cohen & Knoll, 2012; Cohen et al., 2017), provide qualitative evidence that aqueous phosphate reached water column concentrations high enough to offer an ecological opportunity to eukaryotic organisms. Viewed alongside available geochemical data, these observations suggest a marked shift in marine phosphate concentrations may have occurred during the early Tonian (i.e., after ca. 900 Ma) (Reinhard et al., 2017; Guilbaud et al., 2020).

To provide new observational constraints on aqueous P concentrations in Precambrian shallow water settings, we examined the concentration, speciation, and distribution of phosphorus in non-skeletal carbonate sediments from multiple Tonian basins using a combination of optical and electron microscopy, solid state Nuclear Magnetic Resonance (NMR), and synchrotron-based X-ray Fluoresence ($\mu$-XRF) imaging and X-ray Absorption Near Edge Structure (XANES) spectroscopy. We focused on carbonate rocks deposited during the later Tonian period (ca. 850 to 750 Ma) in order to test the hypothesis that aqueous P concentrations, qualitatively inferred from microfossil evidence (Cohen et al., 2017; Moczydłowska et al., 2018; Riedman et al., 2021), may in fact be quantitatively retrieved from non-skeletal carbonate sedimentary rocks more broadly. Here, we place these new microanalytical data in an aqueous geochemical framework to unravel the behaviour of aqueous phosphate during the formation and diagenesis of mid-Neoproterozoic carbonate rocks, and consider the implications of these findings for the nature of the Neoproterozoic P-cycle, and for eukaryotic evolution.

## 2 Geological setting

To investigate phosphorus geochemistry and mineralogy in Tonian rocks, we targeted three well-preserved carbonate-dominated successions (Figure 1), each of which is considered to represent open marine platform deposition; these have prominently featured in several reconstructions of global Neoproterozoic seawater chemistry (Halverson et al., 2005; Macdonald et al., 2010). These successions intermittently record subtidal to peritidal sedimentation in tidal flat to lagoonal environments (Knoll & Swett, 1990; Halverson et al., 2007, 2017).

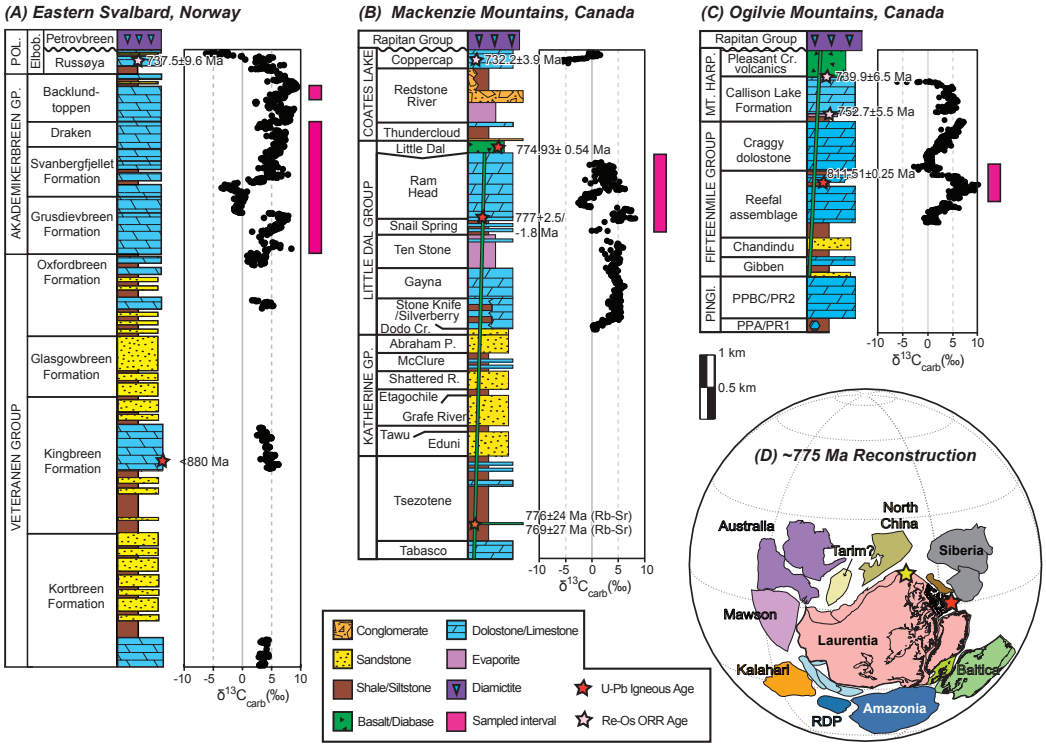


**Figure 1.** Generalized stratigraphy of carbonate-dominated successions examined in this study (A-C), and paleogeographic reconstruction (D) for ca. 775 Ma (Li et al., 2008), with approximate positions of sampled stratigraphy. GP.- Group; POL - Polarisbreen Group; Elbob.- Elbobreen Formation; Shattered R.- Shattered Range Formation; Abraham P. - Abraham Plains Formation; Dodo Cr. - Dodo Creek Formation; Pingl. - Pinguicula Group; Mt. Harp. - Mt. Harper Group; PPA/PR1 - Pinguicula unit A (unit PR1); PPBC/PR2 - Pinguicula units B and C (unit PR2); RDP - Rio de Plata craton; ORR - organic rich rock.

The Tonian Akademikerbreen Group of the Eastern basement domain of Svalbard, Norway, is a ca. 1350–2500m thick carbonate-dominated succession that was deposited at tropical latitudes within a thermally subsiding extensional basin from ca. 830–740 Ma (Wilson, 1961; Knoll & Swett, 1990; Maloof et al., 2006; Halverson et al., 2007, 2017, 2022). It is composed of the Grusdievbreen, Svanbergfjellet, Draken, and Backlundtoppen formations, in stratigraphically ascending order (Wilson, 1961; Knoll & Swett, 1990; Halverson et al., 2007, 2017), and the lower Grusdievbreen and Svanbergfjellet formations record the complete Bitter Springs carbon isotope excursion (CIE) at ca. 810–800 Ma (Figure S1; Halverson et al., 2005; Maloof et al., 2006; Halverson et al., 2007; Swanson-Hysell et al., 2015; Halverson et al., 2017; Cohen et al., 2017).

Analyses were also conducted on samples from the Tonian Fifteenmile Group of the western Ogilvie Mountains, which spans the Yukon (Canada)–Alaska (USA) border. Sampled outcrops included measured sections from both the Tatonduk (Mount Slipper) and Coal Creek inliers (Strauss et al., 2015; Cohen et al., 2017; Macdonald et al., 2017). Previously named the Upper Tindir Group (Macdonald et al., 2010), the Fifteenmile Group was deposited in an intracratonic extensional basin (Strauss et al., 2015; Macdonald et al., 2017). Rhenium-Osmium (Re-Os) geochronology from black, organic-rich shale in the Fifteenmile Group at Mount Slipper provides a depositional age of 810.7 ± 5.8 Ma (Cohen et al., 2017), and zircon U/Pb isotope dilution-thermal ionization mass spectrometry (ID-TIMS) from a tuff in the Fifteenmile Group in the Coal Creek inlier provides an age of 811.5 ± 0.25 Ma ca. 50 m below where $\delta^{13}C$ values begin to decrease as part of the Bitter Springs CIE (Macdonald et al., 2010).

The Fifteenmile Group of the Tatonduk Inlier comprises more than 350 m of stromatolitic dolostone and an additional ca. 500 m of black shale interbedded with quartz sandstone and minor carbonate that are assigned to the Reefal assemblage (Figure S2). The samples analyzed here correspond with the fossiliferous zones in the upper strata of the Reefal assemblage that predate the onset of the Bitter Springs CIE as described by Cohen et al. (2017). These strata consist of ca. 60 m of interbedded planar-laminated lime mudstone, calcareous black and gray shale, and sparse tabular-clast conglomerate and calcisiltite interbedded with discontinuous matrix-supported rudstone and chert nodules that contain apatitic-scale fossils, or ASMs (which also occur in the carbonate matrix; Macdonald et al., 2010; Cohen & Knoll, 2012; Cohen et al., 2017).

The Fifteenmile Group of the Coal Creek Inlier has been subdivided into the Gibben and Chandindu formations and the overlying Reefal assemblage (Macdonald et al., 2011, 2017). The Reefal assemblage contains platform and distal foreslope facies dominated by stromatolite reefs and intertidal to supratidal carbonate facies, including dark grey limestone microbialite indicative of lagoonal depositional settings, dolomitic microbialite indicative of supratidal settings, and abundant grainstone indicative of supratidal and proximal reef settings (Macdonald et al., 2011, 2017). Subtidal carbonate mudstone intervals that contain abundant molar tooth structures are also present within facies dominated by talus reef breccias that are indicative of upper foreslope to lagoonal settings (Macdonald et al., 2011, 2017).

Analyses were also conducted on samples from the Tonian Little Dal Group of the Mackenzie Mountains, Northwest Territories, Canada (Figure S3; Aitken, 1981; Halverson, 2006; Wörndle et al., 2019). The Little Dal Group is part of the Mackenzie Mountains Supergroup, which was deposited in an intracratonic extensional or sag basin. Based on U-Pb ages from detrital zircons in the underlying Katherine Group and diabase U-Pb zircon dates within the unconformably overlying Little Dal Basalts, the Little Dal Group was deposited between ca. 775–1005 Ma, (Morris & Aitken, 1982; Milton et al., 2017). The Little Dal Basalts have been correlated with the ca. 775-780 Ma Gunbarrel large igneous province (Dudas & Lustwerk, 1997; Harlan et al., 2003; Halverson, 2006). The Bitter Springs CIE is also archived in the upper Snail Spring and lower Ram Head formations (Halverson, 2006; Wörndle et al., 2019). The Little Dal Group is a mixed carbonate-siliciclastic succession

that consists of shale, limestone, dolostone, evaporites and sandstone with local major reef complexes (Figure S3). The Snail Spring Formation consists of mudstone with interbedded siltstone and quartz arenite overlain by laminated and reefal carbonates that were deposited in a shallow marine environment (Aitken, 1981; Wörndle et al., 2019). The overlying Ram Head Formation consists of stromatolites and ooid grainstone that were deposited on a high energy carbonate platform (Aitken, 1981; Turner et al., 1993; Turner & Long, 2008; Wörndle et al., 2019).

## 3 Materials and Methods

In order to evaluate the dominant modes and relative timing of phosphate deposition from Tonian seas, for each succession we asked: (1) at what concentrations is P present in different depositional and diagenetic components? (2) what minerals host P identified in the samples? (3) how is P spatially distributed among sedimentary and diagenetic components? To address (1) above, we targeted a total of 275 samples from the three successions. For each sample, bulk P content was determined for powders micro-drilled from a variety of depositional and diagenetic fabrics. To address (2), a subset of these powders was examined with $^{31}$P, $^{19}$F, and $^{1}$H solid state NMR to identify and quantify the host phases of P. To address both (2) and (3), corresponding thin sections were examined with optical microscopy, scanning electron microscopy with energy dispersive X-ray microanalysis (SEM-EDS), and $\mu$-XRF (for Mg, Si, P, Ca, Mn, Fe, and Sr), and XANES spectroscopy at the P- and Fe K-edges at the Stanford Synchrotron Radiation Lightsource beamlines 14-3 and 2-3, respectively. Experiment parameters, calibration, and data reduction procedures for each of these methods are detailed in the following sections.

### 3.1 Analysis of bulk carbonate-associated P

In order to determine bulk $PO_4$ concentrations of micro-drilled powders, powdered carbonate rock samples were digested in 10 mL of 1 molal HCl for 24 hours. To fix pH to the desired rage, 2.425 mL aliquots of this solution were added to 2.575 mL of 1 molal NaOH before diluting with deionised milliQ water, and then spiked with tetrasodium EDTA. Total dissolved phosphate analyses of the resulting solutions was performed spectrophotometrically using the ascorbic acid method (Phosver3 Ascorbic Acid Method 8048, Hach Lange), whereby orthophosphate present in the solution is reacted with molybdate in an acid medium to produce a mixed phosphate/molybdate complex (Baird et al., 2017). The complex then becomes reduced by ascorbic acid, yielding an intense molybdenum blue color that was measured at 880 nm using a HACH DR2800 spectrophotometer (Baird et al., 2017).

### 3.2 Solid state $^{31}$P, $^{19}$F, and $^{1}$H NMR

The $^{31}$P and $^{19}$F MAS/NMR spectra were acquired at Stony Brook University with a 400 MHz (9.4 T) Varian Inova spectrometer operating at 161.9 and 376.2 MHz, respectively. The directly-excited (DE) $^{31}$P spectra were acquired at a spinning rate of 5 kHz with a Chemagnetics-type probe assembly configured with a 7.5 mm (o.d.) spinning system. The $Si_3N_4$ rotors employed do not yield a detectable $^{31}$P NMR signal. A 5 $\mu$s excitation pulse ($56^o$) and 20 s relaxation delay were used to accumulate 9000-12000 scans for each spectrum. The $^{1}$H $\rightarrow$ $^{31}$P CP/MAS experiments were conducted with the same configuration, using 8 $\mu$s $90^o$ $^{1}$H excitation pulses, 31.25 kHz spin lock for a 2 ms contact time, and a linear ramp of the $^{31}$P transverse field of approximately $\pm$ 5 kHz about the first sideband match condition. The relaxation delay was 2 s and the number of scans taken was typically 120,000. The $^{19}$F spectra were acquired at a 10.5 kHz spinning rate using a 4 mm (o.d.) spinning system, with 4 $\mu$s pulses ($72^o$) separated by 20 s relaxation delays for 8,000-20,000 scans. The $^{19}$F chemical shifts are reported with respect to neat $CFCl_3$; those for $^{31}$P were referenced to an external standard of hydroxylapatite, taken to be +2.8 ppm from 85% $H_3PO_4$.

### 3.3 Synchrotron $\mu$XRF and XANES

Phosphorus and iron K-edge $\mu$-XRF maps and XANES spectroscopy were collected at beamlines 14-3 and 2-3, respectively, at SSRL, SLAC National Accelerator Laboratory. The top of the white line of a Durango flourapatite mineral powder at 2152.05 eV was used to calibrate the monochromoator to the P K-edge at BL14-3, while the first derivative of an Fe foil (7112 eV) was used to calbirate the monochromator at BL2-3 to the Fe K-edge. The X-ray beam at both beamlines was focused by Kirkpatrick-Baez mirrors to ca. 5 $\mu$m spot size. Samples were measured at room temperature in a He-purged chamber to decrease $O_2$ levels to <0.1 % at BL14-3 (to reduce X-ray attenuation in air at low X-ray energies), or in air at BL2-3. Maps were collected slightly above the P and Fe K-edge at 2160 and 7200 eV, respectively, and were processed in the MicroAnalysis Toolkit (Webb et al., 2011) by applying a gaussian distribution function to average the intensity over a 5 pixel area in order to reduce noise. Points for XANES spectroscopy were chosen based on hotspots of P within different carbonate fabrics. Initially, one XANES spectrum was collected on each point and assessed for quality. Spectra containing diffraction peaks were not chosen as points to collect repeat scans. Repeat XANES spectra (ranging from 2-6 repeats) were collected based on the signal to noise ratio observed in preliminary XANES spectrum. Due to the presence of diffraction peaks from the sample in a number of XANES spectra, the peak area of the elements in the maps were fit using the multi-channel analysis tool in the MicroAnalysis Toolkit (Webb et al., 2011) to remove the scatter contribution from total P maps. XANES spectra were processed in SIXPACK (Webb, 2005) and Athena (Ravel & Newville, 2005) software packages where repeat measurements were averaged to improve signal to noise ratio, background subtracted by fitting a line to the pre-edge region and normalized by fitting a second order polynomial to the post-edge region with an edge step of 1 at E0.

### 3.4 Scanning electron microscopy and energy dispersive X-ray microanalysis (SEM-EDS)

Scanning Electron Microscope (SEM) analyses of highly polished, carbon coated thin sections were performed using a FEI Quanta 650 Emission Gun operated at an accelerating voltage of 15 kV under high vacuum with a dwell time of 10 $\mu$s. The SEM is also equipped with an Energy Dispersive X-Ray detector to facilitate semi-quantitative chemical analysis via Energy Dispersive Spectroscopy (EDS) by AZtec (Oxford Instruments) with a 50 mm detector, aperture of 3 and spot size of 4 using an approximate 2nA beam current.

### 3.5 Compilation and statistical analysis of sedimentary geochemical data

The Phase 1 Sedimentary Geochemistry and Paleoenvironments Project (SGP) database comprises approximately 90,000 samples, each with multiple associated geochemical analytes, from throughout Earth history (Farrell et al., 2021). Here, we used weighted bootstrap resampling of these data to produce trends of P and TOC in fine grained, non-carbonate mudstones from 1000 to 500 Ma. Prior to resampling, we extracted and filtered data using the work flow described in Mehra et al. (2021). We enforced a minimum absolute age uncertainty of 10 Ma for each sample. To identify mudstones, we ran samples through an initial lithological filter (i.e., selecting only those samples with metadata that matched a pre-selected list of lithologies); following this step, we removed any carbonate- and phosphate-rich mudstones by excluding those samples with Ca values greater than 10 ppm and $P_2O_5$ values greater than 1 wt% (Mehra et al., 2021). Finally, we resampled all remaining data (n = 9406), using a 10 Ma bin size to calculate statistics (e.g., 2.5 and 97.5 uncertainty bounds).

# 4 Results

## 4.1 Stratigraphic variability in P concentrations

Determination of bulk P from micro-drilled carbonate components shows that each carbonate-dominated succession exhibits bulk $PO_4$ ranging from a minimum of a few hundred to a few thousand ppm (Figures S1-S3). The concentration of bulk $PO_4$ through Tonian carbonate successions is irregular, likely arising from variations in carbonate lithofacies or mineralogy, sedimentation rates, and the effects of diagenesis.

The Akademikerbreen Group, Svalbard, Norway, (Figure 1) consists of the predominantly limestone-dominated (with minor dolostone) Grusdievbreen and Svanbergfjellet formations, which record the deposition of carbonate mud, lithoclasts and stromatolites in a largely subtidal storm-influenced carbonate ramp (Knoll & Swett, 1990; Halverson et al., 2017). Elemental data (i.e., Mn, Sr, Fe, Ca, Mg), O- and Sr-isotope data, and I/[Ca + Mg] data together reflect only limited meteoric diagenetic alteration within these two formations, consistent with excellent preservation of primary depositional fabrics (Halverson et al., 2007; Wörndle et al., 2019). The overlying Draken Formation comprises mainly dolorudstone, dolograinstone (including ooids) and microbial dolomudstone intervals puctuated by stromatolitic horizons, reflecting shallow subtidal to supratidal deposition (Knoll & Swett, 1990; Fairchild et al., 1991; Halverson et al., 2017). These strata are overlain by the Backlundtoppen Formation, which is made up of dolograinstone and microbial dolomudstone, in addition to ooilitic grainstones and black laminated lime mudstones. The dolomite that dominates the Draken and Backlundtoppen formations is largely fabric retentive and likely syndepositional to early diagenetic in origin (Fairchild et al., 1991; Halverson et al., 2007). Bulk elemental concentrations (i.e., Mn, Sr, Fe, Ca, Mg, I/[Ca + Mg]) and C-, O- and Sr-isotopic data together reflect only limited diagenetic alteration within these formations, consistent with excellent preservation of primary depositional fabrics (Halverson et al., 2007; Wörndle et al., 2019). In addition, the stratigraphic intervals examined do not contain evidence for evaporite minerals, their pseudomorphs, or other sedimentary structures indicative of evaporative conditions.

The Akademikerbreen Group is characterised by relatively high average bulk [$PO_4$] of several hundred ppm throughout the Grusdievbreen, Svanbergfjellet, Draken, and Backlundtoppen formations (Figure S1). Bulk [$PO_4$] generally increases as the succession shallows upward from the Grusdievbreen through the Svanbergfjellet formations, reaching maximum values in an interval associated with stromatolitic bioherms, dolomitic mudstones, and very fine-grained grainstones of the Svanbergfjellet Formation (Figure S1). Elevated bulk $PO_4$ typically, but not exclusively, corresponds with more negative $\delta^{13}C$ isotopic values, and a relative increase in $PO_4$ concentration is observed through the Bitter Springs C-isotope excursion (CIE). Although no correlation between bulk [$PO_4$] and [Mn]/[Sr] ratio is evident (Figure S1), high [$PO_4$] often, though not exclusively, occurs with elevated Mg/Ca ratios in the Grundiesvebreen and Svanbergfjellet formations (Figure S1). This relationship is not apparent in the Draken Formation.

The interval of the Fifteenmile Group of the Ogilvie Mountains, Yukon, Canada, targeted here comprises ca. 60m of interbedded planar-laminated lime mudstone, calcareous black and grey shale, and sparse tabular-clast conglomerate at the Mount Slipper locality (Figure 1; Cohen et al., 2017). These strata overlie ca. 320m of black and grey shale interbedded with minor intervals of calcareous shale, and lime mudstone and massive quartz arenite, which are in turn overlain by ca. 400m of massive clast-supported dolorudstone, dolograinstone, dolowackestone, and minor calcareous shale and lime mudstone (Figure S2). The targeted interval also contains disseminated gypsum and rare carbonate-replaced fabrics, which together may support evidence for distal basinal restriction (Cohen et al., 2017); however, there are no evaporites described within the Fifteenmile Group, only within equivalent strata of the Mackenzie Mountains (Turner & Bekker, 2016). Sedimentary structures indicate that these strata were deposited well below storm wave base in a distal slope setting. Elemental and

O-isotope data indicate limited diagenetic alteration, consistent with excellent preservation of depositional fabrics (Figures S2 and S10; Cohen et al., 2017).

Bulk $PO_4$ through the Fifteenmile Group increases upward with concentrations in excess of 1000s of ppm (Figure S2). Trace element data determined by ICP-MS on bulk digested sample powders (from Cohen et al., 2017) show that P concentrations generally increase with $CaCO_3$ content. The Fifteenmile Group has both higher average and individual $PO_4$ concentrations relative to the Akademikerbreen Group, and Fifteenmile Group carbonates appear to exhibit some stratigraphic variability in $PO_4$, with lower concentrations corresponding with a predominance of dolomite. This difference between dolomite and calcite may result from crystal chemical constraints on P-incorporation and/or the effects of early marine diagenesis. There is no clear correlation between $\delta^{13}C$ isotopic values and bulk $PO_4$ concentration.

The Little Dal Group of the Mackenzie Mountains, Northwest Territories, Canada, comprises seven formations (Figure 1); we targeted the two uppermost of these: the Snail Spring and Ram Head formations. At its base, the Snail Spring Formation comprises siliciclastic mudstone, silstone, and quartz arenite, overlain by shallow marine laminated carbonates. The overlying Ram Head Formation includes higher-energy carbonate strata dominated by abundant stromatolites and oolitic grainstone. Much of this interval of the Little Dal Group has been dolomitised. Elemental data, O- and Sr-isotope data, and I/[Ca + Mg] data indicate that these intervals record much more extensive diagenesis, with more obvious geochemical evidence for meteoric diagenesis and subsequent dolomitization than both the Akademikerbreen and Fifteenmile groups (Figure S3; Halverson et al., 2005, 2007; Wörndle et al., 2019). These data are consistent with common fabric destructive dolomite fabrics observed in thin section.

Bulk $PO_4$ within the Little Dal Group exhibits minimum concentrations of ca. 100 ppm increasing to maximum values ca. 1185 ppm with a mean of ca. 326 ppm (Figure S3); these values are very similar to those recovered from the Akademikerbreen Group. The base of the succession is characterised by high $PO_4$ concentrations which then abruptly decrease. This trend repeats and is followed by an overall increasing trend higher up in the stratigraphic section. The Little Dal Group carbonates do exhibit some stratigraphic variability in which high $PO_4$ corresponds with more negative $\delta^{13}C$ isotopic values, broadly consistent with both the Akademikerbreen and Fifteenmile groups. The Little Dal Group exhibits some lithological variability with high $PO_4$ concentrations of ca. 1185 ppm characterising stromatolitic horizons and the highest bulk [$PO_4$] occurring within microbial and fine-grained dolomudstone facies (Figure S3).

### 4.2 Speciation and distribution of P in Tonian carbonates

The bulk P data can be coupled with additional geochemical and petrographic data to examine the speciation and distribution of P in the well-preserved Akademikerbreen and Fifteenmile groups; these results are compared to identical analyses on horizons displaying clear geochemical evidence for diagenetic alteration within the Little Dal Group. These data indicate clear differences in the speciation and distribution of P between these three successions and enable us to assess the primary distribution of P in these strata.

#### *4.2.1 Akademikerbreen Group*

Solid state $^{31}P$ NMR spectra indicate that the mineral phase that hosts $PO_4$ in the Akademikerbreen Group carbonates is almost exclusively apatite, with a chemical shift of ca. 2.5-2.8 ppm (Figures 2 and 3). $^{19}F$ data further show that the dominant host of F is consistent with a trioctahedral phyllosilicate (talc, as identified in XRD; Figures 2 and 3), even when this phase is not observable petrographically. In addition, the presence of a $^{19}F$ chemical shift of -102 ppm highlights the presence of fluorapatite (Braun & Jana,

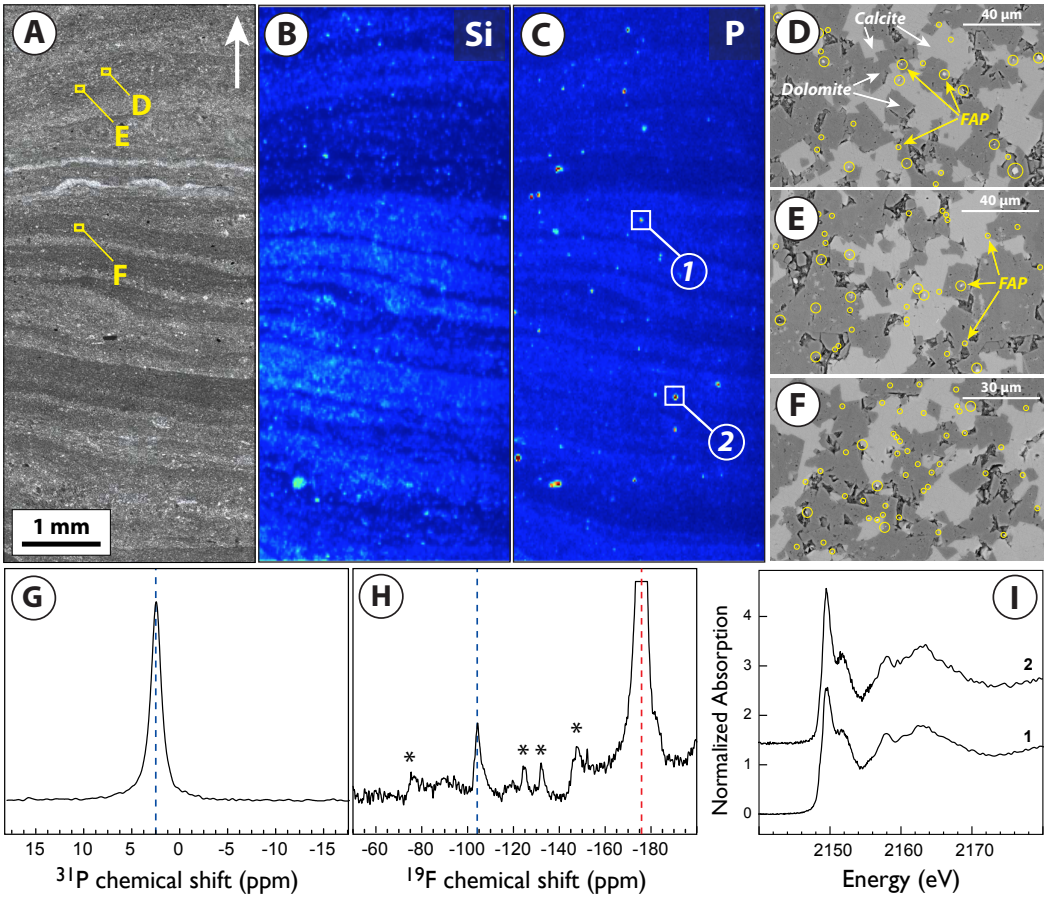


**Figure 2.** Speciation and distribution of P in stromatolitic carbonate from the Tonian Akademikerbreen Group, Svalbard. (A) Petrographic image of thin section (plane polarized light) showing analysis regions. Arrow indicates "stratigraphic up" orientation. (B) Si and (C) P $\mu$-XRF maps showing locations where P-XANES spectra were acquired. Cooler colours correspond to low abundance and warmer colours to high abundance. To aid comparison between figures, colour-concentration relationships for $\mu$-XRF maps are all scaled identically. (D), (E), and (F) Backscattered electron images showing the location of nm-sized fluorapatite crystals relative to carbonate components. (G) $^{31}$P NMR, (H) $^{19}$F NMR (2x vertical scaling; asterisks denote spinning sidebands), and (I) P-XANES spectra showing the presence of absorption edge and post-edge features corresponding to apatite. Numbers correspond to locations in panel (C).

1995), hereafter referred to as FAP throughout (Figures 2 and 3). A weak, broad signal was observed in $^{1}H \rightarrow {}^{31}P$ CP/MAS spectra, which is consistent with the presence of a low concentration of calcite-hosted phosphate, but could also arise from disordered regions near hydroxyl substitutions in the fluorapatite.

Micro-XRF mapping, XANES spectroscopy, and SEM-EDS analysis of Akademikerbreen carbonates reveal that P is spatially distributed in two principal forms: widespread and abundant nanometer-scale apatite crystals, and as calcite-hosted $PO_4$. Disseminated apatite particles ranging from 50-1000 nm in size have been identified across samples characterised by both low (i.e., ca. 200 ppm) and high (i.e., ca. 2000 ppm) bulk [$PO_4$]. Locally high concentrations of P are commonly associated with $PO_4$-rich intraclasts (Figure 3). SEM-EDS analyses reveal that these intraclasts are composed of abundant masses of individual crystals

of FAP (ca. 200 nm at the largest) embedded within a talc cement matrix (Figure 3). The fine-scale mixture of FAP and talc is interpreted to have precipitated during sediment deposition and early diagenesis, and the intraclasts were subsequently re-worked into the surrounding sediments (Figure 3); notably, however, the FAP-talc assemblage also occurs as a pore filling cement. In some cases, FAP crystals and calcite microspar crystals mutually embay one another and FAP crystals are also commonly engulfed by the cores of individual calcite microspar crystals. These relationships indicate that crystallisation of the two minerals occurred contemporaneously (Figure 3).

Micro-XRF, XANES spectroscopy, and SEM-EDS also identified abundant FAP crystals (up to a few hundred nm) and intraclasts trapped and concentrated within and along stromatolitic laminae (e.g., Figure 2). The relationships of these particles with surrounding calcite and dolomite crystals indicate a detrital origin, suggesting that FAP intraclasts and particles were continuously deposited from the water column or through re-working of surrounding sediments across the timespan that stromatolites were accumulating on the seafloor. The lack of a spatial correlation with Si suggests that the supply of phosphate was largely independent of processes that delivered Si to the sediments (Figure 2). In these stromatolitic horizons, individual sub-micron FAP crystals are locally engulfed by calcite and/or dolomite overgrowths on micrite and/or microspar crystals (Figure 3), implying that FAP crystals originally present with primary calcite (as documented above) were subsequently trapped by calcite and/or dolomite during early diagenetic recrystallisation.

Consistent with $^{31}$P NMR data, $\mu$-XRF and XANES also provide evidence for the presence of calcite-hosted $PO_4$ substitutions that are disseminated within $CaCO_3$ calcite microspar cement and petrographically distinct micrite. This calcite-hosted $PO_4$ is characterised by a featureless peak with no post-edge shoulder (in contrast to apatite spectra) and a shift to higher energy values of ca. 0.2–0.3 eV (Figures 2 and 3; Richardson et al., 2022)). These $\mu$-XRF analyses also reveal that the Akademikerbreen carbonates examined here are characterized by elevated Sr in calcite microspar and high background Sr in the carbonate matrix, as well as low Mn/Sr and subtly contrasting distributions of Sr and Mn within thin beds (Figure S5). Fe is present at generally low concentrations within all samples examined and XANES spectra show that Fe is dominantly bound in Fe-silicates, likely of detrital origin, such as biotite and/or chlorite (e.g., Figures S4 and S5).

#### *4.2.2 Fifteenmile Group*

Solid state $^{31}$P and $^{19}$F NMR data from the Fifteenmile Group similarly confirm that P is dominantly hosted as crystalline FAP. In addition, $\mu$-XRF and XANES spectroscopy indicate that P is dominantly located in FAP intraclasts and finely disseminated sub-micron-sized FAP crystals that are abundant in the largely micritic carbonate matrix of host lime mudstone; these components are particularly concentrated along the bedding planes of individual laminae (Figures 4 and 5). As described above, textural relationships with individual calcite and dolomite crystals in the Fifteenmile Group indicate a likely detrital origin for the sub-micron-sized FAP crystals, though these crystals can also be engulfed by calcite and/or dolomite crystals. SEM-EDS and $\mu$-XRF analyses also show that P is commonly hosted in pore-filling FAP cement. These components and relationships were identified in samples obtained from the Tatonduk inlier (Alaska-Yukon border) and from samples obtained from the Coal Creek inlier (Ogilvie Mountains, Yukon). Micro-XRF mapping at the Sr K-edge also reveals that Fifteenmile Group samples are characterized by elevated Sr in the carbonate matrix, with particularly elevated concentrations hosted within calcite microspar intraclasts and cement. Consistent with bulk elemental and O-isotope data described above, low total Mn and low Mn/Sr values are also observed in these strata, which suggests that the intervals examined here have experienced minimal diagenetic recrystallization. Similar to the Akademikerbreen Group, Fe is generally low in concentration and dominantly hosted within silicate phases of likely detrital origin.

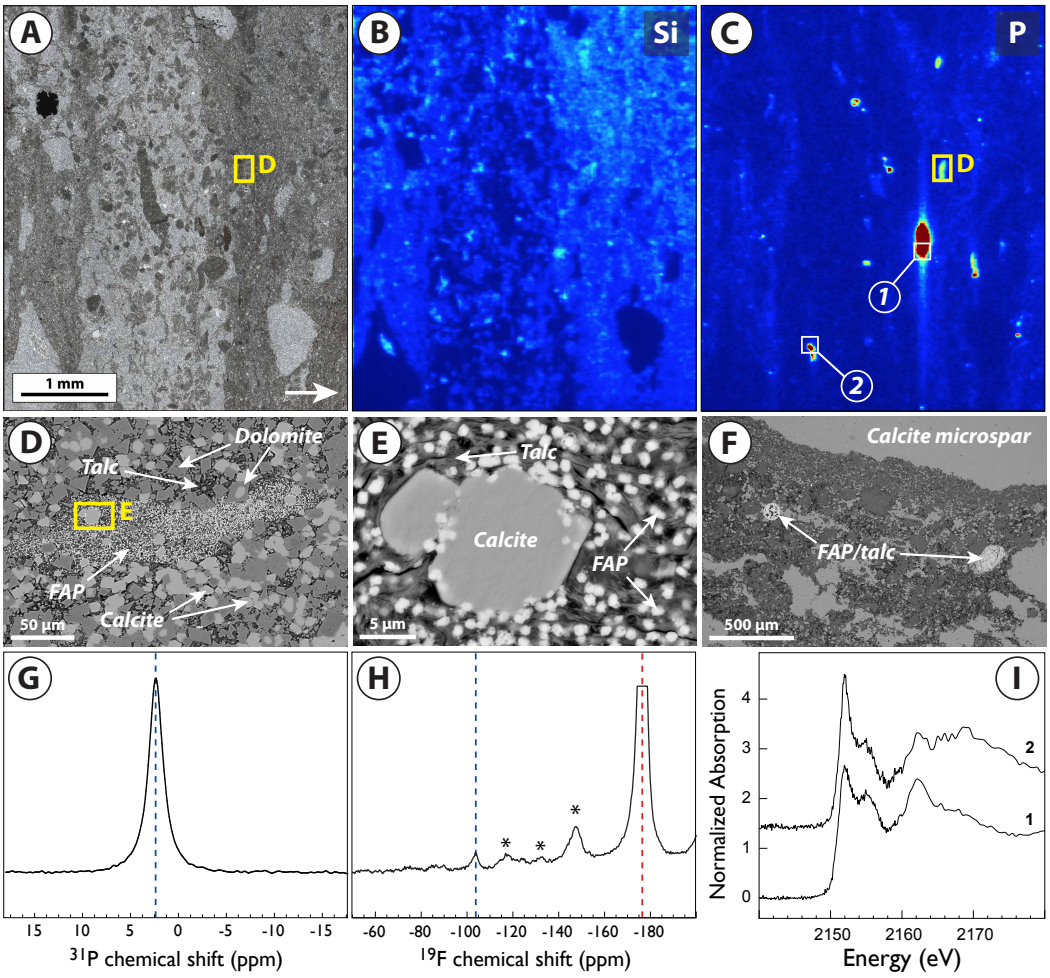


**Figure 3.** Speciation and distribution of P in laminated carbonate mudstone from the Tonian Akademikerbreen Group, Svalbard. (A) Petrographic image of thin section (plane polarized light) showing analysis regions. Arrow indicates "stratigraphic up" orientation. (B) Si and (C) P $\mu$-XRF maps showing locations where P-XANES spectra were acquired. Cooler colours correspond to low abundance and warmer colours to high abundance. To aid comparison between figures, colour-concentration relationships for $\mu$-XRF maps are all scaled identically. (D), (E), and (F) Backscattered electron images showing the location of nm-sized fluorapatite crystals relative to carbonate components. (G) $^{31}$P NMR, (H) $^{19}$F NMR (2x vertical scaling; asterisks denote spinning sidebands), and (I) P-XANES spectra showing the presence of absorption edge and post-edge features corresponding to apatite. Numbers correspond to locations in panel (C).

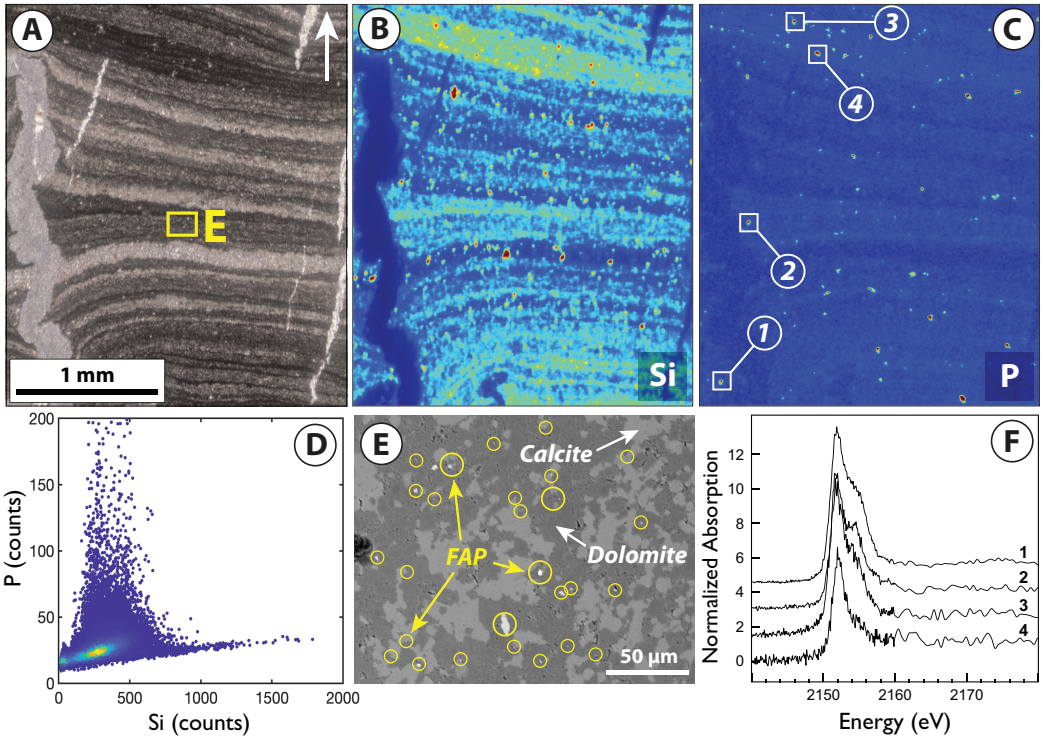


**Figure 4.** Speciation and distribution of P in laminated carbonate mudstones from the Tonian Fifteenmile Group, Coal Creek inlier, Yukon, Canada. (A) Petrographic image of thin section (plane polarized light) showing analysis regions. Note fine-scale lamination and differential compaction of sediments relative to molar-tooth void filled with synsedimentary calcite microspar cement. Arrow indicates "stratigraphic up" orientation. (B) Si and (C) P $\mu$-XRF maps showing locations where P-XANES spectra were acquired. Cooler colours correspond to low abundance and warmer colours to high abundance. To aid comparison between figures, colour-concentration relationships for $\mu$-XRF maps are all scaled identically. (D) Correlation plot of Si and P data obtained from $\mu$-XRF maps showing that P-enriched regions show little correlation with Si-rich regions. (E) Backscattered electron image showing the location of nm-sized fluorapatite (FAP) crystals relative to carbonate components. (F) P-XANES spectra showing the presence of absorption edge and post-edge features corresponding to apatite. Numbers correspond to locations in panel (C).

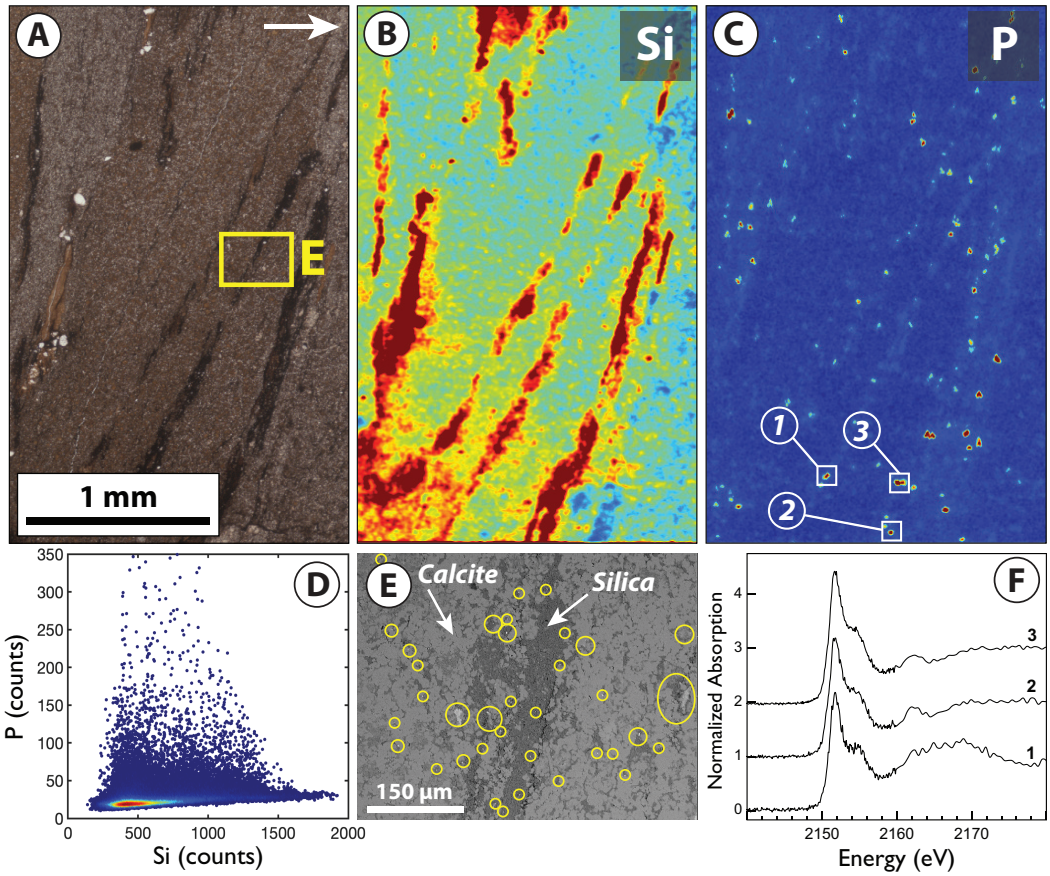


**Figure 5.** Speciation and distribution of P in laminated carbonate mudstones from the Tonian Fifteenmile Group, Mt Slipper, Yukon, Canada. (A) Petrographic image of thin section (plane polarized light) showing analysis regions. Arrow indicates "stratigraphic up" orientation. (B) Si and (C) P $\mu$-XRF maps showing locations where P-XANES spectra were acquired. Cooler colours correspond to low abundance and warmer colours to high abundance. To aid comparison between figures, colour-concentration relationships for $\mu$-XRF maps are all scaled identically. (D) Correlation plot of Si and P data obtained from $\mu$-XRF maps showing that P-enriched regions show little spatial correlation with Si-rich regions. (E) Backscattered electron image showing the location of nm-sized fluorapatite crystals relative to carbonate components. (F) P-XANES spectra showing the presence of absorption edge and post-edge features corresponding to apatite. Numbers correspond to locations in panel (C).

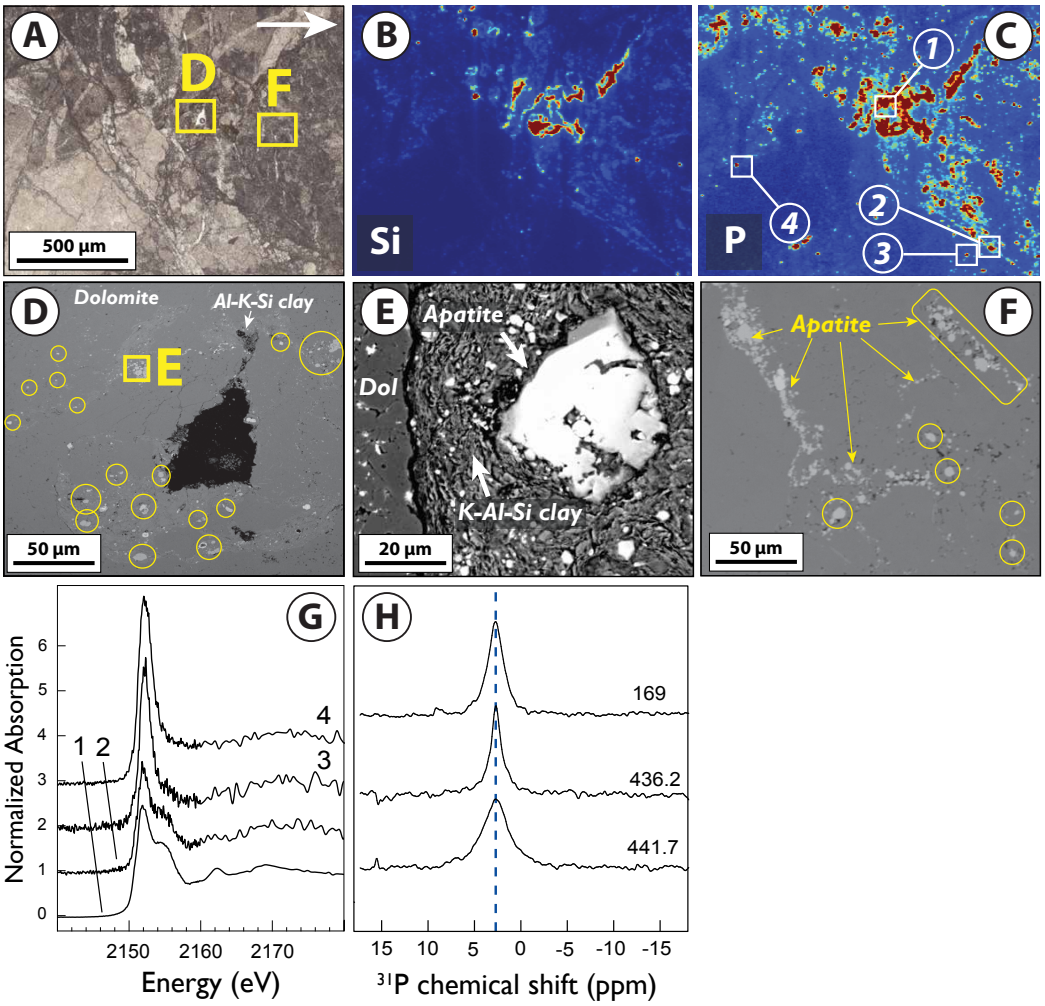


**Figure 6.** Speciation and distribution of P in carbonate mudstones from the Little Dal Group, Northwest Territories, Canada. (A) Petrographic image of thin section (plane polarized light) showing analysis regions. Arrow indicates "stratigraphic up" orientation. (B) Si and (C) P $\mu$XRF maps showing locations where P-XANES spectra were acquired. Note strong spatial correlation between Si and P. (D), (E), and (F) Backscattered electron images showing the location of apatite crystals relative to carbonate components. Note that apatite crystalline masses are distributed in the immediate vicinity of micro-cracks and fractures, which also imparts a "halo" of apatite surrounding a void in the center of (D). (G) P-XANES spectra showing the presence of absorption edge and post-edge features corresponding to apatite. Numbers correspond to locations in panel (C). (H) $^{31}$P solid state NMR of bulk powders extracted from various stratigraphic horizons (stratigraphic height labeled to right. Samples are dominated by a strong apatite peak at ca. 3ppm.

#### *4.2.3 Little Dal Group*

$^{31}$P NMR spectra from selected stromatolitic intervals within the Snail Spring Formation and mudstone and grainstone intervals from the upper Ram Head Formation indicate that apatite predominantly hosts $PO_4$ with a clear $^{31}$P resonance at ca. 2.8 ppm (Figure 6). $^{19}$F data are consistent with fluorapatite (Figure 6). The $^{19}$F peak near -150 ppm could arise from Mg-rich dioctahedral phyllosilicates such as montmorillonite (Huve et al., 1992). Micro-XRF and XANES spectroscopy confirm that P is present as apatite, which is widely distributed within samples dominated by finer grains. Most significantly, however, these data show a markedly different spatial distribution of P than observed in any of the Akademikerbreen or Fifteenmile samples. SEM-EDS shows abundant, but much larger (up to 50 $\mu$m), euhedral apatite crystals that commonly exhibit hexagonal- or lath-shaped morphologies (Figure 6). These larger crystals are mostly concentrated within dolomite and are often associated with K-Al-Si-rich clays (Figure 6). Smaller euhedral apatite crystals (ca. 3-10 $\mu$m) are also abundant and associated with clay minerals, dolomite, and calcite-rich mudstone intervals. However, these smaller crystals display no clear spatial relationship with carbonate components or sedimentary structures that can be confidently attributed to primary deposition. Instead, these crystals are distributed almost exclusively along micro-fracture networks (Figure 6). Larger apatite crystals and crystal masses are commonly concentrated, in some cases with K-Al-Si-rich clay, where these microfractures coalesce to form pore space (Figure 6). These relationships suggest that post-depositional diagenetic processes, including recrystallisation, served as a major control on the spatial distribution of P, even in samples that do not display extensive evidence for fabric-destructive dolomitization.

## 5 Discussion

Our new geochemical and microanalytical data show that the examined Tonian carbonate successions are generally associated with high concentrations of $PO_4$, especially when compared to modern carbonate sediments (Dodd et al., 2021). This association includes several components: (1) individual $PO_4$ substitutions within the calcite and/or dolomite structure (i.e., "calcite- or dolomite-hosted" phosphate), (2) individual crystals of FAP (reaching hundreds of nm in size) of intraformational origin, (3) authigenic FAP-talc precipitates that fill pores and are occasionally re-distributed as intraclasts, and (4) diagenetically remobilized P. To set these results in a sedimentological and biogeochemical context, we discuss constraints on the dynamics of Tonian $CaCO_3$ sedimentation and diagenesis, and on P sources to Tonian carbonates. We then combine these observations with experimental and theoretical geochemical data to constrain minimum and maximum [$PO_4$] in Tonian shallow seas. Finally, we consider controls on marine P bioavailability and implications for the early-middle Neoproterozoic Earth system.

### 5.1 $CaCO_3$ and P deposition in Tonian carbonate successions

Leveraging decades of sedimentological and stratigraphic observations, in addition to recent theoretical and experimental geochemical constraints, our analyses contribute to an increasingly detailed picture of the chemical and physical processes driving early-middle Neoproterozoic carbonate sedimentation. First, as for other carbonate successions of similar age, our observations show that synsedimentary calcite microspar served as a principal building block from which subtidal carbonate grainstone and mudstone accumulated (James et al., 1998). Microspar clasts and grainstone lags dominate these successions, which reflects the erodibility of the sediment shortly after microspar precipitated, and, in turn minimal seafloor cementation beyond intermittent microspar precipitation (James et al., 1998; Cantine et al., 2019; Kriscautzky et al., 2022). In fact, SEM-cathodoluminescence (SEM-CL) imaging shows that individual particles of lime mud exhibit identical size, morphology, and cathodoluminescence characteristics to crystals bound in microspar clasts (Figures S9-S11). These crystals may comprise up to 90% of the fine-grained sediment (e.g., Figures 5 and S10),

or they may be mixed with intraformational silica and dolomite where it may account for up to 60% of the sediment (e.g., Figures 4 and S11). SEM-CL data also show that microspar crystals commonly became dolomitized as they were physically transported to shallower environments (Figure S9).

Microspar is powerful in constraining $CaCO_3$ and P deposition because petrographic and geochemical data indicate that it was initially formed from contemporaneous seawater (James et al., 1998; Frank & Lyons, 1998; Bishop & Sumner, 2006; Zhou et al., 2020; Strauss & Tosca, 2020). Microspar precipitation has been widely documented to have occurred before appreciable compaction of the surrounding sediment (i.e., Figure 4), and while the sediment itself was susceptible to physical re-working (Figures 2, 3, 4, 5; James et al., 1998; Frank & Lyons, 1998; Bishop & Sumner, 2006; Zhou et al., 2020; Strauss & Tosca, 2020). This expression in turn requires substantial and rapid fluid flow within the uppermost portions of the sediment, consistent with geochemical mass balance constraints (Bishop & Sumner, 2006; Spear et al., 2014). Carbonate carbon $\delta^{13}C$ values from $CaCO_3$ microspar are also typically identical to contemporaneous sedimentary components (i.e., ooids, micrite, stromatolites, and intergranular cements; Frank & Lyons, 1998; Halverson et al., 2017; Zhou et al., 2020).

Further insight into $CaCO_3$ and P deposition can be leveraged from recent experiments that have investigated the chemistry required for microspar precipitation. This work shows that in the presence of an effective inhibitor to the direct nucleation of both calcite and aragonite, $CaCO_3$ precipitation will instead proceed through the formation of an amorphous calcium magnesium carbonate (ACMC) precursor, which may rapidly transform to crystalline $CaCO_3$ (i.e., Mg-calcite and/or monohydrocalcite) depending on the Mg/Ca of the solution (Roest-Ellis et al., 2021). This pathway provides a mechanism to explain the distinctive crystal size distribution of calcite microspar, the observation of spheroidal cores, its relative Sr enrichment, the lack of petrographic evidence for a former aragonite precursor, and its association with authigenic Mg-silicates that require high pH and therefore alkalinity (Strauss & Tosca, 2020; Roest-Ellis et al., 2021). Although the relatively high $CaCO_3$ saturation states required to generate the ACMC precursor to microspar (Strauss & Tosca, 2020; Roest-Ellis et al., 2021) appear inconsistent with minimal evidence for penecontemporaneous seafloor cementation (Figure 5; Kriscautzky et al., 2022), these experiments have shown that in the presence of inhibitors to $CaCO_3$ precipitation (i.e., $\mu$mol/kg concentrations of phosphate), direct calcite and aragonite nucleation is effectively arrested and carbonate growth rates decrease by orders of magnitude (Mucci, 1986; Roest-Ellis et al., 2021). In this chemical regime, ACMC sets the threshold for $CaCO_3$ precipitation and its formation exhibits no dependence on pre-existing surfaces, consistent with energetic predictions (Roest-Ellis et al., 2021). Thus, ACMC (and thus microspar) is expected to have initially formed where physical and/or chemical conditions surpassed its saturation in response to fluctuations in temperature, pressure, and/or carbonate chemistry (Roest-Ellis et al., 2021).

In this context, sub-micron sized crystallites of FAP must have originated when depositional settings locally surpassed the requisite nucleation threshold for octacalcium phosphate (OCP). This is because OCP is widely understood to serve as a precursor to marine apatite crystallization owing to kinetic inhibition of direct apatite nucleation by seawater $Mg^{2+}$ (VanCappellen, 1991; Golubev et al., 1999; Gunnars et al., 2004; Oxmann & Schwendenmann, 2014). It follows that because OCP solubility is minimized with increasing pH, precipitation events that yielded microspar and/or talc were also most likely to have nucleated OCP (Figure 3). In addition, given sedimentological and petrographic evidence reflecting sustained re-working of carbonate sediments at the seafloor, the preservation of sub-micron scale FAP particles indicates that the seawater in which it was transported must have maintained saturation with respect to FAP in order to avoid complete particle dissolution (Supporting Information).

### 5.2 P sources during carbonate sedimentation

The detailed picture of Tonian carbonate sedimentation described above provides a framework to evaluate possible origins of P in shallow-marine systems. Although early diagenetic remineralization of organic matter ($C_{org}$) serves as a principal vector through which P is recycled and ultimately deposited in modern sediments (Ingall & Jahnke, 1994; VanCappellen & Ingall, 1994), diverse observations indicate that the pervasive FAP particles distributed within Tonian carbonates were ultimately derived from contemporaneous seawater. First, consistent with Tonian-Cryogenian carbonates worldwide (Sperling & Stockey, 2018; Johnston et al., 2012), there is very little preservation of organic matter across all carbonate successions targeted in this study. Although low organic matter concentrations might be interpreted to reflect efficient and near complete diagenetic $C_{org}$ remineralization, the geochemical consequences of microbial respiration are incompatible with constraints on $CaCO_3$ sedimentation and on the speciation and distribution of associated metabolites. Specifically, aerobic respiration of organic matter yields one mole of DIC per mole of C respired, yet leaves alkalinity effectively unchanged. This outcome, in turn, decreases $CaCO_3$ saturation and commonly promotes $CaCO_3$ dissolution, especially in shallow temperate regions of the modern seafloor. Therefore, aerobic respiration is unlikely to have provided the bulk of P to Tonian carbonate sediments because of the sustained high $CaCO_3$ saturation and high pH required for the textures and mineral assemblages documented across these Tonian carbonate successions (Tosca et al., 2011; Strauss & Tosca, 2020; Roest-Ellis et al., 2021).

Microanalytical data also indicate anaerobic microbial metabolisms were unlikely to have provided substantial P to Tonian carbonate sediments. For example, although microbial iron reduction can be an efficient alkalinity pump, mass balance considerations demand that significant quantities of $Fe^{2+}$ be released to accompany this process. At the $CaCO_3$ supersaturation (and associated DIC and alkalinity) required to promote microspar and talc precipitation (Tosca et al., 2011; Strauss & Tosca, 2020; Roest-Ellis et al., 2021), even minimal amounts of $Fe^{2+}$ would be immediately and quantitatively precipitated as siderite (Jiang & Tosca, 2019). Extensive characterisation of the concentration and distribution of Fe in Tonian carbonates through $\mu$-XRF, XANES, and SEM-EDS shows that it is principally hosted at minor to trace concentrations and dominantly within detrital silicate minerals such as chlorite and/or biotite (e.g., Figures S4 and S5). These data also show that pyrite is relatively rare within the intervals investigated here, indicating that microbial sulfate reduction of organic matter likely played a minor role in providing P to the depositional system. These observations suggest that aqueous phosphate is instead likely to have been supplied to the sediment column directly by seawater.

### 5.3 Geochemical constraints on shallow marine [$PO_4$]

The mineral assemblages and textural relationships documented in Tonian carbonate successions provide rare and quantitative constraints on phosphate concentrations of the fluids from which carbonate and phosphate minerals were derived. First, the formation, sustained physical re-working, and eventual deposition of sub-micron FAP particles in carbonate sediments requires persistent saturation with respect to FAP to prevent complete dissolution. This fact provides a minimum constraint on Tonian phosphate concentrations. Because it contains $CO_3$ ions within its structure, FAP solubility has been shown to vary as a function of carbonate ion concentration in solution (Jahnke, 1984), which allows [$PO_4$] at solubility equilibrium to be determined as a function of temperature, carbonate chemistry (i.e., saturation state, $\Omega_{\mathrm{Calcite}}$), and [Ca] (Supporting Information). Our calculations show that in order for the finest FAP particles (50-100 nm in size as resolvable by SEM) to have been precipitated, transported, deposited, and preserved, seawater phosphate concentrations (as total phosphate, [$PO_{4,Tot}$]) were, at a minimum, between 3-20 $\mu$mol/kg if it was commonly at or near saturation with respect to ACMC (as required by the continuous formation of synsedimentary calcite microspar; Figure 7; Supporting Information). Available

constraints on FAP dissolution rates (and their uncertainties) at pH ranges appropriate for marine carbonate sedimentation indicate that if seawater [$PO_{4,Tot}$] dropped below these concentrations, the finest FAP particles would completely dissolve in 2-20 years (Supporting Information; Figure S7), generally similar to or shorter than, timescales associated with complete lithification of the modern shallow seafloor in carbonate depositional environments (Christ et al., 2015). However, even modern timescales of seafloor cementation are likely to underestimate the integrated contact time between FAP and Tonian seawater given evidence that the Tonian seafloor remained unlithified for timescales long enough to promote continued physical erosion and reworking (Kriscautzky et al., 2022).

The observation of FAP-talc co-precipitates through the Svanbergfjellet Formation (Figures 3 and S1) implies that seawater phosphate concentrations may have periodically exceeded these minimum estimates. The nucleation of OCP, the precursor to FAP precipitation (Section 5.1), is dependent on temperature, pH, [Ca], and [$PO_4$]. With pH constrained by the presence of talc (requiring a minimum pH of 8.5; Tosca et al., 2011), [$PO_{4,Tot}$] may be estimated as a function of [Ca] and temperature (Supporting Information). Although temperatures are uncertain, three constraints on Tonian marine [Ca] further narrow the maximum range of phosphate required to co-precipitate talc and FAP. First, reaction path models of seawater evaporation as a function of chemistry show that a minimum [Ca] of 6 mmol/kg is required in order to account for the observation of Tonian evaporites where gypsum has precipitated before halite (Strauss & Tosca, 2020). Second, fluid inclusion analyses from marine evaporites derived from the ca. 830 Ma Browne Formation constrain marine [Ca] to within 9-12 mmol/kg at this time (Spear et al., 2014). Finally, the observation that talc-FAP co-precipitates also formed in association with synsedimentary microspar (Figure 3) places unique constraints on the equilibrium carbonate system as well as [Ca]. The precipitation of $CaCO_3$ and talc require that total alkalinity (ALK) was equal to or higher than 2[Ca] because the precipitation of $CaCO_3$ removes alkalinity in a 2:1 molar ratio, yet pH must have remained high enough for both minerals to precipitate (Strauss & Tosca, 2020). In addition, the requirement for ACMC nucleation in order to generate calcite microspar places an additional constraint on the carbonate system and [Ca] because Roest-Ellis et al. (2021) observed that the nucleation threshold for ACMC closely corresponds to its solubility. Combining these three constraints (i.e., pH 8.5, ALK>2[Ca], and ACMC saturation) yields solutions for the equilibrium carbonate system in addition to a [Ca] of 18 mmol/kg (Figures 7 and S6; Supporting Information). These findings in turn indicate that shallow Tonian seawater locally reached maximum total phosphate concentrations of 33-94 $\mu$mol/kg depending on temperature and salinity (Figure 7).

### 5.4 Why were Tonian shallow seas periodically phosphate-rich?

From a biogeochemical cycling perspective, increases in [$PO_4$] require marine P input fluxes to have increased, and/or P burial fluxes to have decreased; available data suggest that the early-middle Neoproterozoic phosphorus cycle featured episodes of both phenomena. First, the breakup of the supercontinent Rodinia (between ca. 850 and ca. 720 Ma), chronicled in part by the emplacement of large igneous provinces (LIPs), was likely to have substantially increased P delivery fluxes to the oceans (Figure 8) through enhanced subaerial chemical weathering (Horton, 2015; G. M. Cox et al., 2016; Syverson et al., 2021), which may have led to increases in the relative rates of continental versus seafloor weathering (Sharoni & Halevy, 2023), and/or increased hydrothermal activity. For example, the upwelling mantle plume activity that drove Rodinia breakup would have served as a powerful crustal heat source that promoted increased hydrothermal P fluxes (in part reflected by early Tonian ore deposits; Pirajno & Santosh, 2015), especially in association with anoxic or suboxic seas (Syverson et al., 2021). Additionally, the solutes supplied by the chemical weathering of mafic LIPs are also clearly archived in the $^{87}Sr/^{86}Sr$ record (G. M. Cox et al., 2016; Goddéris et al., 2017), while increased mafic detrital fluxes to marine mudstones are reflected in regional Nd isotopic datasets (G. M. Cox et al., 2016). This unusually high P influx, potentially unprecedented in Earth's history, may have been sustained for over ca. 100 million

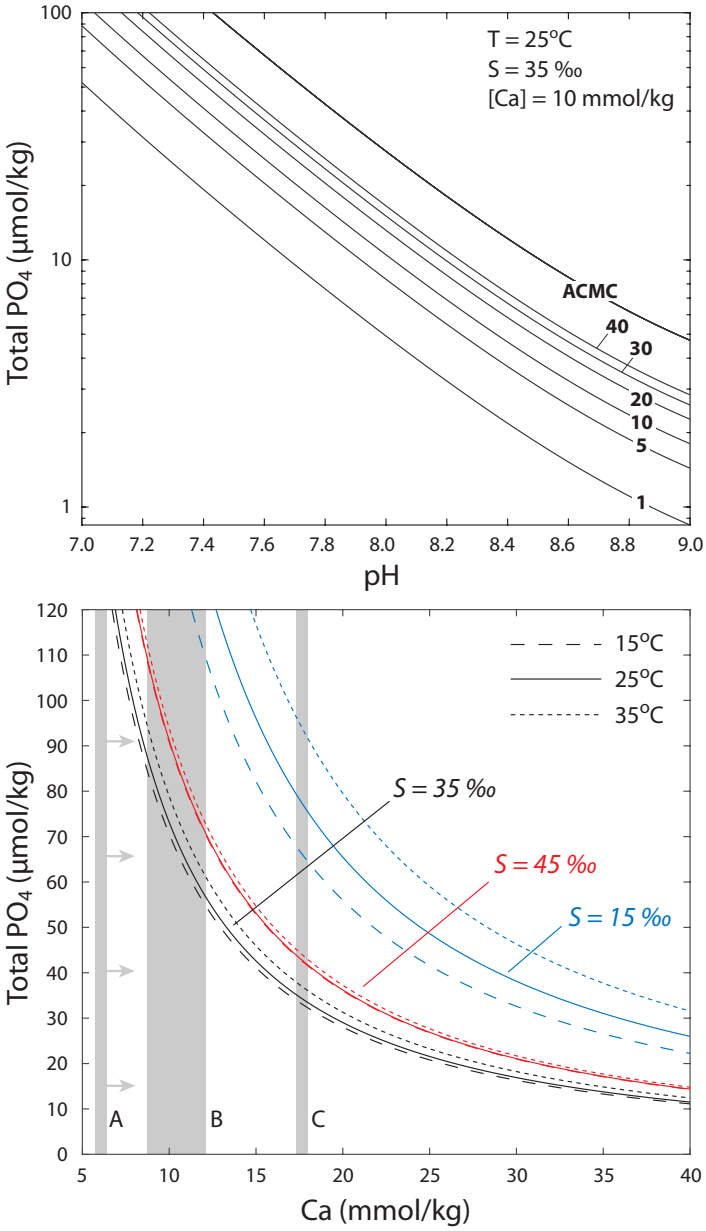


**Figure 7.** Geochemical constraints on phosphate concentration of Tonian shallow seas. Top: Minimum phosphate concentrations required to preserve pervasive FAP particles hundreds of nm in size (Figures 3,2,4,5). Concentrations correspond to solubility equilibrium with respect to FAP as a function of [$CO_3$], expressed in terms of the saturation state relative to calcite ($\Omega_{\mathrm{Calcite}}$). The ACMC curve denotes saturation with respect to amorphous Ca-Mg carbonate, which has been shown to serve as a precursor to synsedimentary calcite microspar, and account for mineralogical, geochemical, and textural characteristics (Strauss & Tosca, 2020; Roest-Ellis et al., 2021). Bottom: Maximum phosphate concentrations required to generate talc-apatite co-precipitates (Figure 3) as a function of [Ca], temperature, and salinity (S). Three constraints on Tonian marine [Ca] are shown (grey bars): (A) reaction path constraints on gypsum-before-halite evaporites of Tonian age (Strauss & Tosca, 2020), (B) fluid inclusion constraints from marine halite deposited within the ca. 830 Ma Browne Formation (Spear et al., 2014), and (C) solubility constraints imposed by talc-microspar assemblages within the ca. 805-788 Ma Svanbergfjellet Formation.

years (Horton, 2015; G. M. Cox et al., 2016). In support of this hypothesis, our statistical analysis of the P concentration in marine mudstones through this same time interval shows a first-order correlation between the bulk P concentration of shales and the quantity of P hosted within Neoproterozoic LIPs (which may also approximate pulses of mantle plume activity), suggesting that these provinces, in addition to hydrothermal contributions, may have dominated P input fluxes across much of the later Tonian (Figure 8; Horton, 2015).

In addition to increases in P delivery fluxes, low P burial efficiency may also have contributed to high marine [$PO_4$] (Tyrrell, 1999; Fennel et al., 2005; Laakso et al., 2020). Over geological timescales, P is ultimately buried as FAP, Fe-associated P, and in organic matter that has escaped remineralization (Poulton, 2017), but there is little direct evidence supporting decreases in FAP and/or Fe-associated P burial through the late Proterozoic. Although chemical influences on FAP precipitation (i.e., [Ca], [$CO_3$], [F] or pH) may have modulated P burial efficiency through time, sustained decreases in FAP burial require corresponding decreases in [Ca], [$CO_3$], and/or pH; available constraints on Tonian carbonate sedimentation offer limited support for such shifts (see Sections 5.1 and 5.3; Strauss & Tosca, 2020; Trower, 2020; Roest-Ellis et al., 2021). Similarly, decreases in the burial efficiency of Fe-oxide-associated P are not supported by current constraints on ocean-atmosphere redox. Proterozoic $pO_2$ levels are not well constrained, but it is widely thought that the Neoproterozoic witnessed a shifting redox structure and progressive oxidation of the deep ocean with the loss of sulfidic and ferruginous conditions (Sperling et al., 2015; Stolper & Bucholz, 2019); some geochemical data indicate that ventilation of the oceans may have begun as early as the Tonian (Turner & Bekker, 2016; Cole et al., 2016), but may not have been complete until the Paleozoic (Stolper & Bucholz, 2019). Consistent with this, recent U-isotope data from Tonian carbonates indicate that shallow seas were commonly anoxic (Zhang et al., 2022), but few data indicate that Tonian seas and/or sediments featured the sulfidic conditions capable of decreasing net Fe-associated P burial compared to earlier and/or later intervals (Ingall & Jahnke, 1994; VanCappellen & Ingall, 1994; Sperling et al., 2015; Poulton, 2017). In fact, although persistently anoxic and ferruginous Proterozoic waters are expected to have scavenged P as the insoluble Fe(II)-phosphate vivianite (Derry, 2015), experiments and models have shown that vivianite is orders of magnitude more soluble in anoxic seawater than previously estimated (Brady et al., 2022), making it unlikely that early diagenetic precipitation served to limit bottom water phosphate concentrations.

High marine [$PO_4$] may have been promoted instead by low $C_{org}$ burial efficiency, either through (1) decreased $C_{org}$ preservation in sediments, and/or (2) low primary production and export from the surface ocean. However, there is little available evidence to support secular shifts that would render the Tonian as an interval characterised by uniquely poor $C_{org}$ preservation in comparison to both earlier and later intervals. First, a distinct increase in baseline $\delta^{13}C$ values, beginning at ca. 900 Ma and continuing through to ca. 750 Ma (Halverson et al., 2018), suggests preservation and burial of $C_{org}$ increased through much of the Tonian (Canfield et al., 2020). In addition, although inherently challenging to relate directly to the extent of $C_{org}$ preservation through time, the Tonian carbonate $\delta^{13}C$ record is mirrored by a pronounced increase in the TOC concentration of shales even though the Neoproterozoic Era as a whole features, on average, relatively low TOC concentrations relative to older and younger intervals (Figure 8; Sperling & Stockey, 2018).

Available evidence, therefore, supports the conclusion that in order for shallow marine [$PO_4$] to have remained high through at least some intervals of the Tonian, the supply of aqueous $PO_4$ must have occasionally outpaced biological utilisation in shallow water depositional environments. One simple possibility could be that the Tonian biosphere was characterised by inherently low rates of primary production (Crockford et al., 2018). For example, if several major N-fixing planktonic cyanobacterial lineages had yet to evolve in the early Tonian (Sánchez-Baracaldo et al., 2021), then it is possible that the efficient internal recycling of P within mat-dominated communities (e.g., Canfield & Marais, 1993) may have collectively represented a minor sink for shallow water phosphate. Alternatively, however,

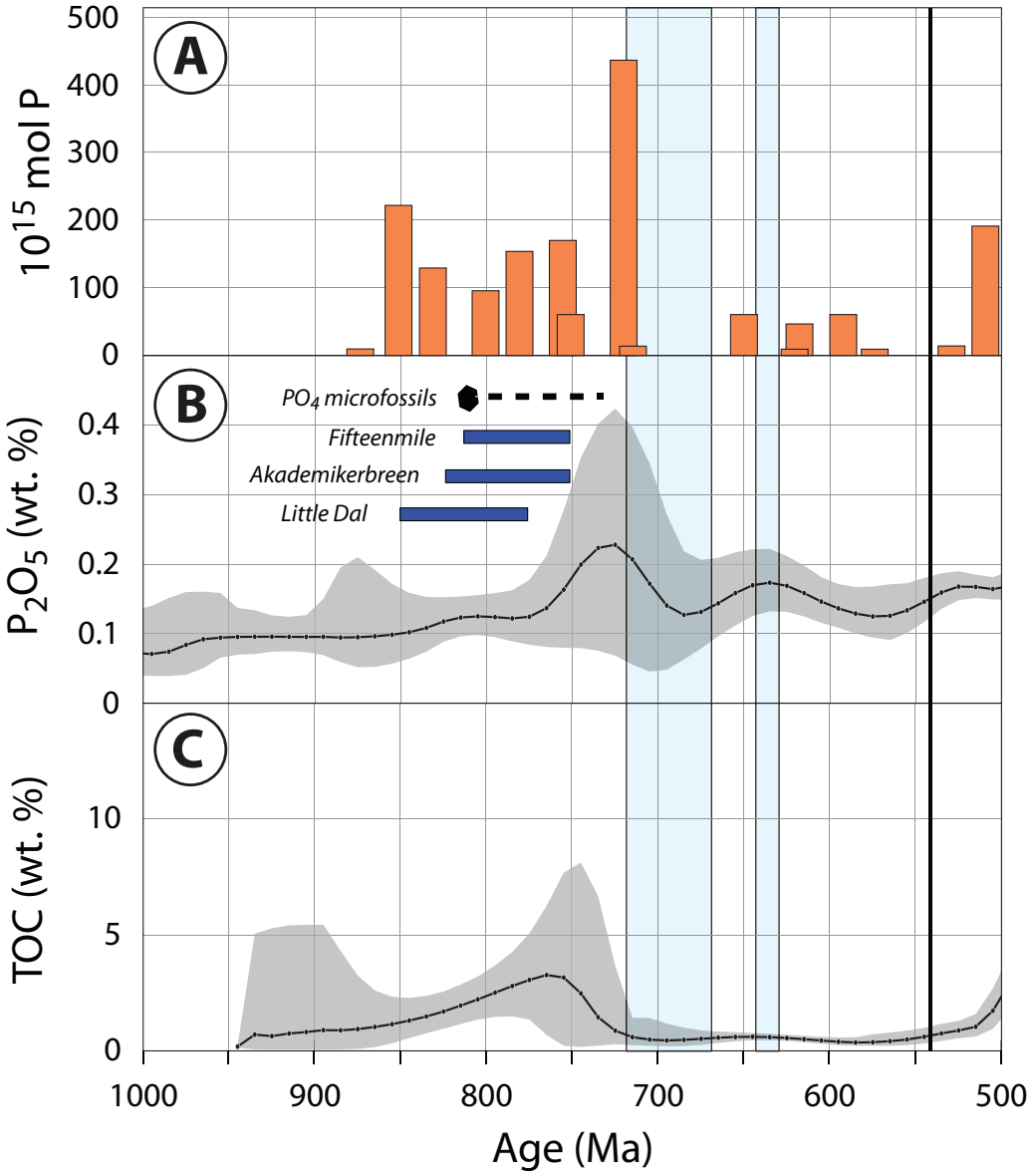


**Figure 8.** (A) Estimated P content for Neoproterozoic and Cambrian large igneous provinces (LIPs; from Horton (2015)). (B) Resampled filtered shale-hosted $P_2O_5$ and total organic carbon (TOC) concentration (C) through the late Proterozoic and early Cambrian derived from the Phase 1 Sedimentary Geochemistry and Paleoenvironments Project (SGP) database. Black points represent resampled mean calculated for 10 Ma bins, and grey envelope shows 2.5% and 97.5% uncertainty bounds (Mehra et al., 2021). Black hexagon denotes stratigraphic age of apatite scale microfossils (Cohen et al., 2017), and black dashed line denotes approximate range of phosphatic scale microfossils associated with vase shaped microfossil assemblages (Riedman et al., 2021). Blue bars denote approximate stratigraphic distribution of samples analyzed in this study. Vertical light blue bars indicate Sturtian and Marinoan glaciations, and vertical black bar denotes Precambrian-Cambrian boundary.

multiple lines of evidence suggest that increases in marine P supply may have triggered a cascade of biogeochemical feedbacks that perturbed nutrient inventories and biospheric production in shallow water environments.

### 5.5 Implications for Tonian biogeochemical cycles and eukaryotic evolution

One immediate consequence of elevated shallow water $PO_4$ concentrations relates to the marine $CaCO_3$ cycle. Experiments have shown that above ca. 1 $\mu$mol/kg, increases in aqueous phosphate concentration translate to order-of-magnitude decreases in the growth rate of pre-existing $CaCO_3$ (Mucci, 1986). Above ca. 12 $\mu$mol/kg, phosphate completely inhibits the nucleation of calcite and aragonite, establishing ACMC solubility as the minimum point at which $CaCO_3$ nucleation can occur (Mucci, 1986; Roest-Ellis et al., 2021). By simulataneously decreasing the shallow-water $CaCO_3$ removal flux and increasing the saturation threshold for $CaCO_3$ precipitation, phosphate-induced $CaCO_3$ inhibition may have promoted large fluctuations in marine carbonate chemistry, especially in the absence of a significant pelagic $CaCO_3$ sink (Ridgwell et al., 2003). Elevated P input fluxes to carbonate depositional environments may have promoted continued increases in alkalinity and pH until depositional environments reached high precipitation thresholds (Roest-Ellis et al., 2021), consistent with the mineralogy and textures of several early-middle Neoproterozoic carbonate successions (James et al., 1998; Strauss & Tosca, 2020; Trower, 2020; Roest-Ellis et al., 2021; Kriscautzky et al., 2022). If that threshold was crossed in multiple basins, comparatively rapid and extensive $CaCO_3$ precipitation may have then driven abrupt decreases in alkalinity and pH, as well as the release of $CO_2$ to the atmosphere. Although the ultimate causes remain debated, this oscillatory mode of carbonate deposition is broadly consistent with the onset of substantial volatility in the carbonate $\delta^{13}C$ record, which commences at ca. 900 Ma (Halverson et al., 2018; Strauss & Tosca, 2020), and also with geochemical reconstructions supporting secular variability in Tonian marine carbonate chemistry and atmospheric $CO_2$ (Strauss & Tosca, 2020).

In addition to driving perturbations to marine carbonate chemistry, climate, and C-isotope partitioning, a kinetically-controlled marine $CaCO_3$ cycle may have impacted the supply of fixed N, which may have periodically sustained phosphate-rich shallow seas. If a bioavailable N pool dominated by $NH_4^+$ was delivered to warm, alkaline, high-pH shallow seas through coastal upwelling, N-loss may have been sustained by at least two mechanisms. First, deprotonation of $NH_4^+$ at elevated pH would have resulted in the persistent loss of bioavailable N through the volatilisation of $NH_3$, with the extent of volatilisation increasing sharply with both pH and temperature (at pH 8.5, seawater carries 5-6x more $NH_3$ for a given [$NH_4^+$ + $NH_3$] concentration than seawater at pH 7.7; Figure S8, Supporting Information). Second, N limitation may have been exacerbated by $NH_3$ toxicity to both benthic and planktonic organisms. For example, photosynthesis, dark respiration, and growth are inhibited by increasing [$NH_3$] because it is thought to interfere with photosystems I and II, the electron transport chain, and the oxygen-evolution complex (Abeliovich & Azov, 1976; Markou et al., 2016). In fact, chlorophyll fluorescence monitoring studies indicate that photosynthetic activity decreases with increasing pH; at pH $\geq$ 8.8, photosynthetic activity can be completely lost in some algal species (Drath et al., 2008; Markou et al., 2016).

At the same time, if shale TOC data and the Tonian $\delta^{13}C$ record reflect increased $C_{org}$ burial, perhaps in response to tectonically-driven increases in P supply, then atmospheric $O_2$ would have necessarily accumulated through much of the Tonian. Sulfate evaporites (Turner & Bekker, 2016) and some geochemical proxies provide support for Tonian oxygenation (Cole et al., 2016), but the magnitude is poorly constrained. Nevertheless, increasing atmospheric $O_2$ may have long-term impacts on N-limitation, and therefore primary productivity. Thermodynamic considerations suggest that ammonia probably dominated the fixed-N pool through the Archean and perhaps much of the Proterozoic (Fennel et al., 2005; Ward et al., 2021), but models predict that before the emergence of the "modern" oxidative N-cycle, initial increases in $O_2$ would have first promoted N-limitation as ammonia was efficiently

converted to nitrite/nitrate, and eventually reduced to $N_2$ gas (Fennel et al., 2005). ~~Recent phylogenetic and molecular clock analyses suggest that N-loss may have been driven entirely by ammonia oxidizing Archea (AOA), whose metabolic activities can also deplete ammonia through anammox in anoxic waters~~. Consistent with this, available sedimentary N-isotope data do appear to record an oxidative signal through the later Tonian, which may reflect an increasing importance of oxidative N-cycling, but further work is required to constrain the availability of fixed N to the Tonian biosphere (Kang et al., 2023). Nevertheless, if increasing oxygenation caused N-limitation to spread beyond shallow water settings, then a literal reading of shale and carbonate records indicates that this progressed through the late Tonian, culminating in a pronounced decrease in shale-hosted TOC concentrations coincident with a precipitous rise in bulk P concentration just prior to the onset of the Sturtian glaciation (Figure 8).

Finally, geochemical constraints on Tonian shallow water settings imply that early eukaryotes may have diversified against a tumultuous environmental backdrop; this may have presented marine ecosystems with new challenges and opportunities. The extended Proterozoic incumbency of cyanobacteria is commonly interpreted in the context of nutrient limitation because eukaryotes cannot effectively compete with prokaryotes under nutrient-limited conditions (Brocks et al., 2017; Reinhard et al., 2017). While there is good evidence to suggest that the biomarker record may not accurately chronicle the rise of eukaryotes to ecological dominance (Pawlowska et al., 2013; Cohen & Kodner, 2022), our data open the possibility that, while serving as a necessary precondition, an expanded P inventory need not itself have driven the rise of eukaryotic algae. In fact, phylogenetic analyses and fossil data suggest that the clade *Archaeoplastida*, which includes both red and green algae, had already evolved by ca. 1000 Ma (Cohen & Kodner, 2022). Because this clade is relatively deeply rooted within the eukaryotic phylogeny, many of the main branches must have also diverged by the beginning of the Tonian Period. However, alongside the evolution of nutrient inventories, abrupt variations in carbonate chemistry and climate may have reconfigured fitness landscapes of microbial ecosystems by introducing fluctuations in the physico-chemical boundary conditions of marine habitats, food and nutrient supplies (including both P and N), and in the $CaCO_3$ saturation states that promote encrustation (Marin et al., 1996). Fossil evidence for eukaryvory (Porter, 2016; Cohen & Riedman, 2018), phosphate biomineralisation (Cohen et al., 2017; Riedman et al., 2021; Cohen & Kodner, 2022) and the construction of recalcitrant structures (Cohen & Kodner, 2022) suggests that the nature and timing of these fluctuations may provide new insight into the ecological dynamics of the Tonian biosphere.

## 6 Conclusions

The data presented here show that well-preserved carbonate rocks may record valuable quantitative constraints on aqueous phosphate concentrations in shallow water settings. In combination with mudstone geochemistry, these data support the possibility that tectonically-driven increases in marine P fluxes may have initiated a regime of kinetically-controlled $CaCO_3$ deposition. Available data suggest that this regime, if triggered synchronously across multiple Tonian seas, may have promoted significant fluctuations in marine carbonate chemistry, atmospheric $pCO_2$, climate, and nutrient inventories. At the same time, however, the mudstone record supports the hypothesis that continued influxes in P may have driven long-term $C_{org}$ burial and oxygenation that in turn may have depleted fixed N for much of the late Tonian biosphere. The emerging narratives from mudstone and carbonate records presents Earth scientists the new challenge of disentangling how nutrient inventories varied across space as well as time. Nevertheless, our results have shown that aside from serving as as a principal nutrient controlling biospheric productivity over geological timescales, interactions between phosphorus, marine carbonate chemistry, and the global C-cycle may hold the key to understanding the mechanisms and feedbacks underpinning Neoproterozoic Earth system change.

## 7 Open Research

The raw analytical data presented in this paper include solid-state NMR, and synchrotron-hosted XANES and $\mu$-XRF data from Tonian carbonate samples. Data and calibrations associated with these analyses are available through the EarthChem Library, Submission ID 2854 [`https://ecl.earthchem.org/view.php?id=2854`], *Research data supporting: Tonian carbonates record phosphate-rich shallow seas* (Tosca, 2023). The dataset also includes MATLAB scripts (as .m files) supporting geochemical calculations presented to constrain phosphate concentrations through mineral assemblages in carbonate samples. Micro-XRF maps were analysed using the Microanalysis Toolkit developed by Webb et al. (2011) [`https://www.sams-xrays.com/smak`]. The peak area of the elements in the maps were fit using the multi-channel analysis tool in the MicroAnalysis Toolkit to remove the scatter contribution from total P maps. XANES spectra were processed in SIXPACK (Webb, 2005) [`https://www.sams-xrays.com/sixpack`] and Athena (Ravel & Newville, 2005) [`https://bruceravel.github.io/demeter/documents/Athena/index.html`] software packages. Geochemical calculations were performed using MATLAB [`https://www.mathworks.com/products/matlab.html`]. Compilation and statistical analysis of sedimentary geochemical data was performed using data from the Sedimentary Geochemistry and Paleoenvironments Project, which is freely available at: `https://sgp-search.io/`. Filtering and analysis procedures for these data are detailed in section 3, and in Mehra et al. (2021).

**Acknowledgments**

We thank Galen Halverson, Marcus Kunzmann, Kristin Bergmann, Tyler Mackey for assistance in the collection of samples in the field and/or the donation of samples for this study, and Katherine Clayton, Iris Buisman, and Jon Wells for analytical support. Akademikerbreen Group samples were collected under permit number RiS-ID-6867, and through logistical support provided by Trond Aasvoll. Use of the Stanford Synchrotron Radiation Lightsource, SLAC National Accelerator Laboratory, is supported by the U.S. Department of Energy (DOE), Office of Science, Office of Basic Energy Sciences under Contract No. DE-AC02-76SF00515. The SSRL Structural Molecular Biology Program is supported by the DOE Office of Biological and Environmental Research, and by the National Institutes of Health (NIH), National Institute of General Medical Sciences (NIGMS) (P41GM103393). The contents of this publication are solely the responsibility of the authors and do not necessarily represent the official views of NIGMS or NIH. We also thank the UK Natural Environment Research Council (NE/M00578X/1), the Leverhulme Trust (PLP-2015-286 to NJT), National Geographic Society (CP-129R-17 to JVS), United States National Science Foundation (EAR-1929597 to JVS), and Alfred P. Sloan Foundation (FG-2021-16053 to JVS) for financial support. NJT thanks the Gordon and Betty Moore Foundation and the California Institute of Technology for generous support and for hosting him in 2022 during the writing of much of this manuscript.

## References

Abeliovich, A., & Azov, Y. (1976). Toxicity of ammonia to algae in sewage oxidation ponds. *Applied and Environmental Microbiology*, *31*(6), 801–806. doi: 10.1128/aem.31.6.801-806.1976

Aitken, J. D. (1981). Stratigraphy and sedimentology of the Upper Proterozoic Little Dal Group, Mackenzie Mountains, Northwest Territories. In F. A. H. Campbell (Ed.), *Proterozoic basins of canada* (Vol. 81-10, pp. 47–71).

Al-Droubi, A., Fritz, B., Gac, J. Y., & Tardy, Y. (1980). Generalized residual alkalinity concept: Application to prediction of the chemical evolution of natural waters by evaporation. *American Journal of Science*, *280*, 560–572.

Baird, R., Eaton, A. D., Rice, E. W., & Bridgewater, L. (2017). *Standard Methods for the Examination of Water and Wastewater* (23rd ed.). American Public Health

Association.

Bishop, J. W., & Sumner, D. Y. (2006, 01). Molar tooth structures of the Neoarchean Monteville formation, Transvaal Supergroup, South Africa. I: Constraints on microcrystalline CaCO3 precipitation. *Sedimentology*, *53*(5), 1049–1068. doi: 10.1111/j.1365-3091.2006.00801.x

Brady, M. P., Tostevin, R., & Tosca, N. J. (2022). Marine phosphate availability and the chemical origins of life on Earth. *Nature Communications*, *13*(1), 5162. doi: 10.1038/s41467-022-32815-x

Braun, M., & Jana, C. (1995). 19F NMR spectroscopy of fluoridated apatites. *Chemical Physics Letters*, *245*(1), 19–22. doi: 10.1016/0009-2614(95)00992-d

Brocks, J. J., Jarrett, A. J. M., Sirantoine, E., Hallmann, C., Hoshino, Y., & Liyanage, T. (2017, 01). The rise of algae in Cryogenian oceans and the emergence of animals. *Nature*, *548*(7669), 578–581. doi: 10.1038/nature23457

Canfield, D. E., Knoll, A. H., Poulton, S. W., Narbonne, G. M., & Dunning, G. R. (2020, 02). Carbon isotopes in clastic rocks and the Neoproterozoic carbon cycle. *American Journal of Science*, *320*(2), 97–124. Retrieved from `http://www.ajsonline.org/lookup/doi/10.2475/02.2020.01` doi: 10.2475/02.2020.01

Canfield, D. E., & Marais, D. J. D. (1993). Biogeochemical cycles of carbon, sulfur, and free oxygen in a microbial mat. *Geochimica et Cosmochimica Acta*, *57*(16), 3971–3984. doi: 10.1016/0016-7037(93)90347-y

Cantine, M. D., Knoll, A. H., & Bergmann, K. D. (2019). Carbonates before skeletons: A database approach. *Earth-Science Reviews*, *201*, 103065. doi: 10.1016/j.earscirev.2019.103065

Chien, S.-H. (1972). *Ion-activity products of some apatite minerals* (Unpublished doctoral dissertation).

Christ, N., Immenhauser, A., Wood, R. A., Darwich, K., & Niedermayr, A. (2015). Petrography and environmental controls on the formation of Phanerozoic marine carbonate hardgrounds. *Earth-Science Reviews*, *151*, 176–226. doi: 10.1016/j.earscirev.2015.10.002

Clegg, S. L., & Whitfield, M. (1995, 06). A chemical model of seawater including dissolved ammonia and the stoichiometric dissociation constant of ammonia in estuarine water and seawater from 2 to 40°C. *Geochimica et Cosmochimica Acta*, *59*(12), 2403–2421. Retrieved from `https://www.sciencedirect.com/science/article/pii/0016703795001352` doi: 10.1016/0016-7037(95)00135-2

Cohen, P. A., & Knoll, A. H. (2012, 01). Scale Microfossils from the Mid-Neoproterozoic Fifteenmile Group, Yukon Territory. *Journal of Paleontology*, *86*(5), 775–800. doi: 10.1666/11-138.1

Cohen, P. A., & Kodner, R. B. (2022). The earliest history of eukaryotic life: uncovering an evolutionary story through the integration of biological and geological data. *Trends in Ecology & Evolution*, *37*(3), 246–256. doi: 10.1016/j.tree.2021.11.005

Cohen, P. A., & Riedman, L. A. (2018). It's a protist-eat-protist world: recalcitrance, predation, and evolution in the Tonian–Cryogenian ocean. *Emerging Topics in Life Sciences*, *2*(2), 173–180. doi: 10.1042/etls20170145

Cohen, P. A., Strauss, J. V., Rooney, A. D., Sharma, M., & Tosca, N. (2017, 01). Controlled hydroxyapatite biomineralization in an 810 million-year-old unicellular eukaryote. *Science Advances*, *3*(6), e1700095. doi: 10.1126/sciadv.1700095

Cole, D. B., Reinhard, C. T., Wang, X., Gueguen, B., Halverson, G. P., Gibson, T., ... Planavsky, N. J. (2016). A shale-hosted Cr isotope record of low atmospheric oxygen during the Proterozoic. *Geology*, *44*(7), 555–558. doi: 10.1130/g37787.1

Cox, G. M., Halverson, G. P., Stevenson, R. K., Vokaty, M., Poirier, A., Kunzmann, M., ... Macdonald, F. A. (2016, 01). Continental flood basalt weathering as a trigger for Neoproterozoic Snowball Earth. *Earth and Planetary Science Letters*, *446*, 89–99. Retrieved from `http://dx.doi.org/10.1016/j.epsl.2016.04.016` doi: 10.1016/j.epsl.2016.04.016

Cox, J. D., Wagman, D. D., & Medvedev, V. A. (1989). *CODATA Key Values for Thermodynamics*. Hemisphere Publishing Corp.

Crockford, P. W., Hayles, J. A., Bao, H., Planavsky, N. J., Bekker, A., Fralick, P. W., ... Wing, B. A. (2018, 07). Triple oxygen isotope evidence for limited mid-Proterozoic primary productivity. *Nature*, *559*(7715), 613–616. Retrieved from `http://www.nature.com/articles/s41586-018-0349-y` doi: 10.1038/s41586-018-0349-y

Derry, L. A. (2015, 01). Causes and consequences of mid-Proterozoic anoxia. *Geophysical Research Letters*, *42*(20), 8538–8546. doi: 10.1002/2015gl065333

Dodd, M. S., Zhang, Z., Li, C., Algeo, T. J., Lyons, T. W., Hardisty, D. S., ... Wang, W. (2021). Development of carbonate-associated phosphate (CAP) as a proxy for reconstructing ancient ocean phosphate levels. *Geochimica et Cosmochimica Acta*, *301*, 48–69. doi: 10.1016/j.gca.2021.02.038

Drath, M., Kloft, N., Batschauer, A., Marin, K., Novak, J., & Forchhammer, K. (2008). Ammonia Triggers Photodamage of Photosystem II in the Cyanobacterium Synechocystis sp. Strain PCC 6803. *Plant Physiology*, *147*(1), 206–215. doi: 10.1104/pp.108.117218

Dudas, F. O., & Lustwerk, R. L. (1997). Geochemistry of the Little Dal basalts: continental tholeiites from the Mackenzie Mountains, Northwest Territories, Canada. *Canadian Journal of Earth Sciences*, *34*(1), 50–58. doi: 10.1139/e17-004

Erwin, D. H., Laflamme, M., Tweedt, S. M., Sperling, E. A., Pisani, D., & Peterson, K. J. (2012, 01). The Cambrian Conundrum: Early Divergence and Later Ecological Success in the Early History of Animals. *Science*, *334*(6059), 1091–1097. doi: 10.1126/science.1206375

Fairchild, I. J., Knoll, A. H., & Swett, K. (1991, 01). Coastal lithofacies and biofacies associated with syndepositional dolomitization and silicification (Draken Formation, Upper Riphean, Svalbard). *Precambrian Research*, *53*(3-4), 165–197. doi: 10.1016/0301-9268(91)90071-h

Farrell, C., Samawi, R., Anjanappa, S., Klykov, R., Adeboye, O. O., Agic, H., ... Sperling, E. A. (2021). The Sedimentary Geochemistry and Paleoenvironments Project. *Geobiology*, *19*(6), 545–556. doi: 10.1111/gbi.12462

Fennel, K., Follows, M., & Falkowski, P. G. (2005, 01). The co-evolution of the nitrogen, carbon and oxygen cycles in the proterozoic ocean. *American Journal of Science*, *305*(6-8 SPEC. ISS.), 526–545. doi: 10.2475/ajs.305.6-8.526

Frank, T. D., & Lyons, T. W. (1998). "Molar-tooth" structures: A geochemical perspective on a Proterozoic enigma. *Geology*, *26*(8), 683–686. doi: 10.1130/0091-7613(1998)026⟨0683:mtsagp⟩2.3.co;2

Goddéris, Y., Hir, G. L., Macouin, M., Donnadieu, Y., Hubert-Théou, L., Dera, G., ... Halverson, G. P. (2017, 01). Paleogeographic forcing of the strontium isotopic cycle in the Neoproterozoic. *Gondwana Research*, *42*, 151–162. doi: 10.1016/j.gr.2016.09.013

Golubev, S. V., Pokrovsky, O. S., & Savenko, V. S. (1999, 09). Unseeded precipitation of calcium and magnesium phosphates from modified seawater solutions. *Journal of Crystal Growth*, *205*(3), 354–360. Retrieved from `https://www.sciencedirect.com/science/article/pii/S0022024899002195` doi: 10.1016/s0022-0248(99)00219-5

Guidry, M. W., & Mackenzie, F. T. (2003, 08). Experimental study of igneous and sedimentary apatite dissolution: Control of pH, distance from equilibrium, and temperature on dissolution rates. *Geochimica et Cosmochimica Acta*, *67*(16), 2949–2963. Retrieved from `https://www.sciencedirect.com/science/article/pii/S0016703703002655` doi: 10.1016/s0016-7037(03)00265-5

Guilbaud, R., Poulton, S. W., Thompson, J., Husband, K. F., Zhu, M., Zhou, Y., ... Lenton, T. M. (2020, 04). Phosphorus-limited conditions in the early Neoproterozoic ocean maintained low levels of atmospheric oxygen. *Nature Geoscience*, *13*(4), 296–301. Retrieved from `http://www.nature.com/articles/s41561-020-0548-7` doi: 10.1038/s41561-020-0548-7

Gunnars, A., Blomqvist, S., & Martinsson, C. (2004, 11). Inorganic formation of apatite in brackish seawater from the Baltic Sea: An experimental approach. *Marine Chemistry*, *91*(1-4), 15–26. Retrieved from `https://www.sciencedirect.com/science/article/pii/S0304420304001252` doi: 10.1016/j.marchem.2004.01.008

Gunnarsson, I., & Arnórsson, S. (2000, 01). Amorphous silica solubility and the thermo-

dynamic properties of H4SiO°4 in the range of 0° to 350°C at Psat. *Geochimica et Cosmochimica Acta*, *64*(13), 2295–2307. doi: 10.1016/s0016-7037(99)00426-3

Gunnarsson, I., Arnórsson, S., & Jakobsson, S. (2005, 01). Precipitation of poorly crystalline antigorite under hydrothermal conditions. *Geochimica et Cosmochimica Acta*, *69*(11), 2813–2828. doi: 10.1016/j.gca.2005.02.001

Halverson, G. P. (2006, 01). A Neoproterozoic Chronology. *Neoproterozoic Geobiology and Paleobiology*, 231–271. Retrieved from http://link.springer.com/10.1007/1-4020-5202-2_8 doi: 10.1007/1-4020-5202-2_8

Halverson, G. P., Dudás, F. , Maloof, A. C., & Bowring, S. A. (2007, 01). Evolution of the 87Sr/86Sr composition of Neoproterozoic seawater. *Palaeogeography, Palaeoclimatology, Palaeoecology*, *256*(3-4), 103–129. doi: 10.1016/j.palaeo.2007.02.028

Halverson, G. P., Hoffman, P. F., Schrag, D. P., Maloof, A. C., & Rice, A. H. N. (2005, 01). Toward a Neoproterozoic composite carbon-isotope record. *Bulletin of the Geological Society of America*, *117*(9-10), 1181–1207. doi: 10.1130/b25630.1

Halverson, G. P., Kunzmann, M., Strauss, J. V., & Maloof, A. C. (2017, 01). The Tonian-Cryogenian transition in Northeastern Svalbard. *Precambrian Research*, *319*(October 2017), 79–95. Retrieved from https://doi.org/10.1016/j.precamres.2017.12.010 doi: 10.1016/j.precamres.2017.12.010

Halverson, G. P., Porter, S. M., & Gibson, T. M. (2018, 01). Dating the late Proterozoic stratigraphic record. *Emerging Topics in Life Sciences*, *2*(2), 137–147. Retrieved from http://www.emergtoplifesci.org/lookup/doi/10.1042/ETLS20170167 doi: 10.1042/etls20170167

Halverson, G. P., Shen, C., Davies, J. H. F. L., & Wu, L. (2022). A Bayesian Approach to Inferring Depositional Ages Applied to a Late Tonian Reference Section in Svalbard. *Frontiers in Earth Science*, *10*. doi: 10.3389/feart.2022.798739

Harlan, S. S., Heaman, L., LeCheminant, A. N., & Premo, W. R. (2003). Gunbarrel mafic magmatic event: A key 780 Ma time marker for Rodinia plate reconstructions. *Geology*, *31*(12), 1053–1056. doi: 10.1130/g19944.1

Hoffman, P. F., Abbot, D. S., Ashkenazy, Y., Benn, D. I., Brocks, J. J., Cohen, P. A., ... Warren, S. G. (2017, 01). Snowball Earth climate dynamics and Cryogenian geology-geobiology. *Science Advances*, *3*(11), e1600983–e1600983. Retrieved from http://advances.sciencemag.org/lookup/doi/10.1126/sciadv.1600983 doi: 10.1126/sciadv.1600983

Horton, F. (2015, 06). Did phosphorus derived from the weathering of large igneous provinces fertilize the neoproterozoic ocean? *Geochemistry, Geophysics, Geosystems*, *16*(6), 1723–1738. Retrieved from http://doi.wiley.com/10.1002/2015GC005792 doi: 10.1002/2015gc005792

Huve, L., Delmotte, L., Martin, P., Dred, R. L., Baron, J., & Saehr, D. (1992). 19F MAS-NMR Study of Structural Fluorine in Some Natural and Synthetic 2:1 Layer Silicates. *Clays and Clay Minerals*, *40*(2), 186–191. doi: 10.1346/ccmn.1992.0400208

Ingall, E., & Jahnke, R. (1994, 06). Evidence for enhanced phosphorus regeneration from marine sediments overlain by oxygen depleted waters. *Geochimica et Cosmochimica Acta*, *58*(11), 2571–2575. Retrieved from https://www.sciencedirect.com/science/article/pii/0016703794900337 doi: 10.1016/0016-7037(94)90033-7

Jahnke, R. A. (1984, 01). The synthesis and solubility of carbonate fluorapatite. *American Journal of Science*, *284*(1), 58–78. Retrieved from http://www.ajsonline.org/cgi/doi/10.2475/ajs.284.1.58 doi: 10.2475/ajs.284.1.58

James, N. P., Narbonne, G. M., & Sherman, A. G. (1998, 01). Molar-tooth carbonates: shallow subtidal facies of the mid- to late Proterozoic. *Journal of Sedimentary Research*, *68*(5), 716–722. doi: 10.2110/jsr.68.716

Jiang, C. Z., & Tosca, N. J. (2019). Fe(II)-carbonate precipitation kinetics and the chemistry of anoxic ferruginous seawater. *Earth and Planetary Science Letters*, *506*, 231–242. doi: 10.1016/j.epsl.2018.11.010

Johansson, O., & Wedborg, M. (1979, 08). Stability constants of phosphoric acid in seawater of 5–40‰ salinity and temperatures of 5–25°C. *Marine Chemistry*, *8*(1),

57–69. Retrieved from https://www.sciencedirect.com/science/article/pii/0304420037990032X doi: 10.1016/0304-4203(79)90032-x

Johnston, D. T., MacDonald, F. A., Gill, B. C., Hoffman, P. F., & Schrag, D. P. (2012, 01). Uncovering the neoproterozoic carbon cycle. *Nature*, *483*(7389), 320–323. Retrieved from http://dx.doi.org/10.1038/nature10854 doi: 10.1038/nature10854

Kang, J., Gill, B., Reid, R., Zhang, F., & Xiao, S. (2023). Nitrate limitation in early Neoproterozoic oceans delayed the ecological rise of eukaryotes. *Science Advances*, *9*(12), eade9647. doi: 10.1126/sciadv.ade9647

Kile, D. E., & Eberl, D. D. (2003, 01). On the origin of size-dependent and size-independent crystal growth: Influence of advection and diffusion. *American Mineralogist*, *88*(10), 1514–1521. doi: 10.2138/am-2003-1014

Knoll, A. H., & Swett, K. (1990). Carbonate deposition during the late Proterozoic Era: an example from Spitsbergen. *American journal of science*, *290-A*, 104–32.

Kriscautzky, A., Kah, L. C., & Bartley, J. K. (2022). Molar-Tooth Structure as a Window into the Deposition and Diagenesis of Precambrian Carbonate. *Annual Review of Earth and Planetary Sciences*, *50*(1), 1–26. doi: 10.1146/annurev-earth-031621-080804

Laakso, T. A., & Schrag, D. P. (2014, 01). Regulation of atmospheric oxygen during the Proterozoic. *Earth and Planetary Science Letters*, *388*, 81–91. Retrieved from http://dx.doi.org/10.1016/j.epsl.2013.11.049 doi: 10.1016/j.epsl.2013.11.049

Laakso, T. A., Sperling, E. A., Johnston, D. T., & Knoll, A. H. (2020, 01). Ediacaran reorganization of the marine phosphorus cycle. *Proceedings of the National Academy of Sciences*, *117*(22), 11961–11967. Retrieved from http://www.pnas.org/lookup/doi/10.1073/pnas.1916738117 doi: 10.1073/pnas.1916738117

Lasaga, A. C. (1998). *Kinetic theory in the earth sciences*. Princeton University Press.

Li, Z., Bogdanova, S., Collins, A., Davidson, A., Waele, B. D., Ernst, R., ... Vernikovsky, V. (2008, 01). Assembly, configuration, and break-up history of Rodinia: A synthesis. *Precambrian Research*, *160*(1-2), 179–210. doi: 10.1016/j.precamres.2007.04.021

Macdonald, F. A., Schmitz, M. D., Crowley, J. L., Roots, C. F., Jones, D. S., Maloof, A. C., ... Schrag, D. P. (2010, 01). Calibrating the Cryogenian. *Science*, *327*(5970), 1241–1243. doi: 10.1126/science.1183325

Macdonald, F. A., Schmitz, M. D., Strauss, J. V., Halverson, G. P., Gibson, T. M., Eyster, A., ... Crowley, J. L. (2017, 01). Cryogenian of Yukon. *Precambrian Research*, *319*(March 2017), 114–143. Retrieved from https://doi.org/10.1016/j.precamres.2017.08.015 doi: 10.1016/j.precamres.2017.08.015

Macdonald, F. A., Smith, E. F., Strauss, J. V., Cox, G. M., Halverson, G. P., & Roots, C. F. (2011, 01). Neoproterozoic and early Paleozoic correlations in the western Ogilvie Mountains, Yukon. In (pp. 161–182).

Maloof, A. C., Halverson, G. P., Kirschvink, J. L., Schrag, D. P., Weiss, B. P., & Hoffman, P. F. (2006, 01). Combined paleomagnetic, isotopic, and stratigraphic evidence for true polar wander from the Neoproterozoic Akademikerbreen Group, Svalbard, Norway. *Bulletin of the Geological Society of America*, *118*(9-10), 1099–1124. doi: 10.1130/b25892.1

Marin, F., Smith, M., Isa, Y., Muyzer, G., & Westbroek, P. (1996, 01). Skeletal matrices, muci, and the origin of invertebrate calcification. *Proceedings of the National Academy of Sciences*, *93*(4), 1554–1559. Retrieved from http://www.pnas.org/cgi/doi/10.1073/pnas.93.4.1554 doi: 10.1073/pnas.93.4.1554

Markou, G., Depraetere, O., & Muylaert, K. (2016). Effect of ammonia on the photosynthetic activity of Arthrospira and Chlorella: A study on chlorophyll fluorescence and electron transport. *Algal Research*, *16*, 449–457. doi: 10.1016/j.algal.2016.03.039

Mehra, A., Keller, C., Zhang, T., Tosca, N., McLennan, S., Sperling, E., ... Strauss, J. (2021). Curation and Analysis of Global Sedimentary Geochemical Data to Inform Earth History. *GSA Today*, *31*(5), 4–10. doi: 10.1130/gsatg484a.1

Millero, F. J., & Pierrot, D. (1998, 01). A chemical equilibrium model for natural waters. *Aquatic Geochemistry*, *4*(1), 153–199. doi: 10.1023/a:1009656023546

Milton, J. E., Hickey, K. A., Gleeson, S. A., & Friedman, R. M. (2017). New U-Pb

constraints on the age of the Little Dal Basalts and Gunbarrel-related volcanism in Rodinia. *Precambrian Research*, *296*, 168–180. doi: 10.1016/j.precamres.2017.04.030

Moczydłowska, M., Pease, V., Willman, S., Wickström, L., & Agić, H. (2018, 01). A Tonian age for the Visingsö Group in Sweden constrained by detrital zircon dating and biochronology: Implications for evolutionary events. *Geological Magazine*, *155*(5), 1175–1189. Retrieved from https://doi.org/10.1017/S0016756817000085 doi: 10.1017/s0016756817000085

Morris, W. A., & Aitken, J. D. (1982). Paleomagnetism of the Little Dal lavas, Mackenzie Mountains, Northwest Territories, Canada. *Canadian Journal of Earth Sciences*, *19*(10), 2020–2027. doi: 10.1139/e82-179

Mucci, A. (1983). The solubility of calcite and aragonite in seawater at various salinities, temperatures, and one atmosphere total pressure. *American Journal of Science*, *283*(7), 780–799. doi: 10.2475/ajs.283.7.780

Mucci, A. (1986). Growth kinetics and composition of magnesian calcite overgrowths precipitated from seawater: Quantitative influence of orthophosphate ions. *Geochimica et Cosmochimica Acta*, *50*(10), 2255–2265. doi: 10.1016/0016-7037(86)90080-3

Oxmann, J. F., & Schwendenmann, L. (2014, 01). Quantification of octacalcium phosphate, authigenic apatite and detrital apatite in coastal sediments using differential dissolution and standard addition. *Ocean Science*, *10*(3), 571–585. Retrieved from www.ocean-sci.net/10/571/2014/ doi: 10.5194/os-10-571-2014

Pawlowska, M. M., Butterfield, N. J., & Brocks, J. J. (2013, 01). Lipid taphonomy in the Proterozoic and the effect of microbial mats on biomarker preservation. *Geology*, *41*(2), 103–106. doi: 10.1130/g33525.1

Pierrehumbert, R., Abbot, D., Voigt, A., & Koll, D. (2011, 01). Climate of the Neoproterozoic. *Annual Review of Earth and Planetary Sciences*, *39*(1), 417–460. Retrieved from http://www.annualreviews.org/doi/10.1146/annurev-earth-040809-152447 doi: 10.1146/annurev-earth-040809-152447

Pirajno, F., & Santosh, M. (2015). Mantle plumes, supercontinents, intracontinental rifting and mineral systems. *Precambrian Research*, *259*, 243–261. doi: 10.1016/j.precamres.2014.12.016

Planavsky, N. J., Asael, D., Rooney, A. D., Robbins, L. J., Gill, B. C., Dehler, C. M., ... Reinhard, C. T. (2022). A sedimentary record of the evolution of the global marine phosphorus cycle. *Geobiology*. doi: 10.1111/gbi.12536

Porter, S. M. (2016). Tiny vampires in ancient seas: evidence for predation via perforation in fossils from the 780–740 million-year-old Chuar Group, Grand Canyon, USA. *Proceedings of the Royal Society B: Biological Sciences*, *283*(1831), 20160221. doi: 10.1098/rspb.2016.0221

Poulton, S. W. (2017, 01). Biogeochemistry: Early phosphorus redigested. *Nature Geoscience*, *10*(2), 75–76. Retrieved from http://www.nature.com/doifinder/10.1038/ngeo2884 doi: 10.1038/ngeo2884

Purgstaller, B., Mavromatis, V., Goetschl, K. E., Steindl, F. R., & Dietzel, M. (2021, 01). Effect of temperature on the transformation of amorphous calcium magnesium carbonate with near-dolomite stoichiometry into high Mg-calcite. *CrystEngComm*, *23*(9), 1969–1981. Retrieved from http://dx.doi.org/10.1039/D0CE01679A doi: 10.1039/d0ce01679a

Ravel, B., & Newville, M. (2005). ATHENA , ARTEMIS , HEPHAESTUS : data analysis for X-ray absorption spectroscopy using IFEFFIT [Software]. *Journal of Synchrotron Radiation*, *12*(4), 537–541. doi: 10.1107/s0909049505012719

Reinhard, C. T., Planavsky, N. J., Gill, B. C., Ozaki, K., Robbins, L. J., Lyons, T. W., ... Konhauser, K. O. (2017, 01). Evolution of the global phosphorus cycle. *Nature*, *541*(7637), 386–389. Retrieved from http://dx.doi.org/10.1038/nature20772 doi: 10.1038/nature20772

Richardson, J. A., Roest-Ellis, S., Phillips, B. L., Strauss, J. V., Webb, S. M., & Tosca, N. J. (2022). Characterization and Geological Implications of Precambrian Calcite-Hosted Phosphate. *Geophysical Research Letters*, *49*(17). doi: 10.1029/2022gl100328

Ridgwell, A. J., Kennedy, M. J., & Caldeira, K. (2003, 01). Carbonate Deposition, Climate Stability, and Neoproterozoic Ice Ages. *Science*, *302*(5646), 859–862. doi: 10.1126/science.1088342

Riedman, L. A., Porter, S. M., & Czaja, A. D. (2021, 02). Phosphatic scales in vase-shaped microfossil assemblages from Death Valley, Grand Canyon, Tasmania, and Svalbard. *Geobiology*, *19*(4), 364–375. Retrieved from https://onlinelibrary.wiley.com/doi/10.1111/gbi.12439 doi: 10.1111/gbi.12439

Roest-Ellis, S., Strauss, J. V., & Tosca, N. J. (2021, 12). Experimental constraints on nonskeletal CaCO3 precipitation from Proterozoic seawater. *Geology*, *49*(5), 561–565. Retrieved from https://pubs.geoscienceworld.org/gsa/geology/article/593675/Experimental-constraints-on-nonskeletal-CaCO3 doi: 10.1130/g48044.1

Sharoni, S., & Halevy, I. (2023). Rates of seafloor and continental weathering govern Phanerozoic marine phosphate levels. *Nature Geoscience*, *16*(1), 75–81. doi: 10.1038/s41561-022-01075-1

Spear, N., Holland, H. D., Garcia-Veígas, J., Lowenstein, T. K., Giegengack, R., & Peters, H. (2014, 01). Analyses of fluid inclusions in Neoproterozoic marine halite provide oldest measurement of seawater chemistry. *Geology*, *42*(2), 103–106. doi: 10.1130/g34913.1

Sperling, E. A., & Stockey, R. G. (2018, 01). The Temporal and Environmental Context of Early Animal Evolution: Considering All the Ingredients of an "Explosion". *Integrative and comparative biology*, *58*(4), 605–622. doi: 10.1093/icb/icy088

Sperling, E. A., Wolock, C. J., Morgan, A. S., Gill, B. C., Kunzmann, M., Halverson, G. P., ... Johnston, D. T. (2015, 01). Statistical analysis of iron geochemical data suggests limited late Proterozoic oxygenation. *Nature*, *523*(7561), 451–454. doi: 10.1038/nature14589

Stolper, D. A., & Bucholz, C. E. (2019, 04). Neoproterozoic to early Phanerozoic rise in island arc redox state due to deep ocean oxygenation and increased marine sulfate levels. *Proceedings of the National Academy of Sciences of the United States of America*, 201821847–201821847. Retrieved from http://www.ncbi.nlm.nih.gov/pubmed/30975756 doi: 10.1073/pnas.1821847116

Stolper, D. A., & Keller, C. B. (2018, 01). A record of deep-ocean dissolved O2from the oxidation state of iron in submarine basalts. *Nature*, *553*(7688), 323–327. Retrieved from http://dx.doi.org/10.1038/nature25009 doi: 10.1038/nature25009

Strauss, J. V., MacDonald, F. A., Halverson, G. P., Tosca, N. J., Schrag, D. P., & Knoll, A. H. (2015, 01). Stratigraphic evolution of the Neoproterozoic Callison Lake Formation: Linking the break-up of Rodinia to the Islay carbon isotope excursion. *American Journal of Science*, *315*(10), 881–944. doi: 10.2475/10.2015.01

Strauss, J. V., & Tosca, N. J. (2020, 01). Mineralogical constraints on Neoproterozoic pCO2 and marine carbonate chemistry. *Geology*, *48*(6), 599–603. doi: 10.1130/g47506.1

Swanson-Hysell, N. L., Maloof, A. C., Condon, D. J., Jenkin, G. R., Alene, M., Tremblay, M. M., ... Haileab, B. (2015, 01). Stratigraphy and geochronology of the Tambien Group, Ethiopia: Evidence for globally synchronous carbon isotope change in the Neoproterozoic. *Geology*, *43*(4), 323–326. doi: 10.1130/g36347.1

Syverson, D. D., Reinhard, C. T., Isson, T. T., Holstege, C. J., Katchinoff, J. A. R., Tutolo, B. M., ... Planavsky, N. J. (2021). Nutrient Supply to Planetary Biospheres From Anoxic Weathering of Mafic Oceanic Crust. *Geophysical Research Letters*, *48*(19). doi: 10.1029/2021gl094442

Sánchez-Baracaldo, P., Bianchini, G., Wilson, J. D., & Knoll, A. H. (2021). Cyanobacteria and biogeochemical cycles through Earth history. *Trends in Microbiology*, *30*(2), 143–157. doi: 10.1016/j.tim.2021.05.008

Tosca, N. J. (2023). Research data supporting: Tonian carbonates record phosphate-rich shallow seas [Dataset]. *Interdisciplinary Earth Data Alliance (IEDA)*. doi: 10.26022/IEDA/112854

Tosca, N. J., Macdonald, F. A., Strauss, J. V., Johnston, D. T., & Knoll, A. H. (2011, 01). Sedimentary talc in Neoproterozoic carbonate successions. *Earth and Planetary Science Letters*, *306*(1-2), 11–22. Retrieved from http://dx.doi.org/10.1016/j.epsl.2011

.03.041 doi: 10.1016/j.epsl.2011.03.041

Trower, E. J. (2020, 01). The Enigma of Neoproterozoic Giant Ooids—Fingerprints of Extreme Climate? *Geophysical Research Letters*, *47*(4), 1–10. doi: 10.1029/2019gl086146

Tung, M. S., Eidelman, N., Sieck, B., & Brown, W. E. (1988, 01). Octacalcium Phosphate Solubility Product from 4 to 37 °C. *Journal of Research of the National Bureau of Standards*, *93*(5), 613–624. Retrieved from ["https://nvlpubs.nist.gov/nistpubs/jres/093/jresv93n5p613_A1b.pdf","http://nvlpubs.nist.gov/nistpubs/jres/093/jresv93n5p613_A1b.pdf"] doi: 10.6028/jres.093.153

Turner, E. C., & Bekker, A. (2016, 01). Thick sulfate evaporite accumulations marking a mid-neoproterozoic oxygenation event (ten stone formation, Northwest territories, Canada). *Bulletin of the Geological Society of America*, *128*(1-2), 203–222. doi: 10.1130/b31268.1

Turner, E. C., & Long, D. G. (2008, 01). Basin architecture and syndepositional fault activity during deposition of the Neoproterozoic Mackenzie Mountains supergroup, Northwest Territories, Canada. *Canadian Journal of Earth Sciences*, *45*(10), 1159–1184. Retrieved from http://www.nrcresearchpress.com/doi/abs/10.1139/E08-062 doi: 10.1139/e08-062

Turner, E. C., Narbonne, G. M., & James, N. P. (1993, 01). Neoproterozoic reef microstructures from the Little Dal Group, northwestern Canada. *Geology*, *21*(3), 259–262. Retrieved from https://pubs.geoscienceworld.org/gsa/geology/article-pdf/21/3/259/3514556/i0091-7613-21-3-259.pdf doi: 10.1130/0091-7613(1993)021⟨0259:nrmftl⟩2.3.co;2

Tutolo, B. M., & Tosca, N. J. (2018, 01). Experimental examination of the Mg-silicate-carbonate system at ambient temperature: Implications for alkaline chemical sedimentation and lacustrine carbonate formation. *Geochimica et Cosmochimica Acta*, *225*, 80–101. Retrieved from http://www.scopus.com/inward/record.url?eid=2-s2.0-85041574296\&partnerID=MN8TOARS doi: 10.1016/j.gca.2018.01.019

Tyrrell, T. (1999). The relative influences of nitrogen and phosphorus on oceanic primary production. *Nature*, *400*(6744), 525–531. doi: 10.1038/22941

VanCappellen, P. (1991). *The formation of marine apatite - A kinetic study* (Unpublished doctoral dissertation).

VanCappellen, P., & Ingall, E. D. (1994, 10). Benthic phosphorus regeneration, net primary production, and ocean anoxia: A model of the coupled marine biogeochemical cycles of carbon and phosphorus. *Paleoceanography*, *9*(5), 677–692. Retrieved from http://doi.wiley.com/10.1029/94PA01455 doi: 10.1029/94pa01455

VanCappellen, P., & Ingall, E. D. (1996). Redox Stabilization of the Atmosphere and Oceans by Phosphorus-Limited Marine Productivity. *Science*, *271*(5248), 493–496. doi: 10.1126/science.271.5248.493

Ward, L. M., Johnston, D. T., & Shih, P. M. (2021, 12). Phanerozoic radiation of ammonia oxidizing bacteria. *Scientific Reports*, *11*(1), 2070–2070. Retrieved from http://www.nature.com/articles/s41598-021-81718-2 doi: 10.1038/s41598-021-81718-2

Webb, S. M. (2005). SIXPack a Graphical User Interface for XAS Analysis Using IFEFFIT [Software]. *Physica Scripta*, 1011. doi: 10.1238/physica.topical.115a01011

Webb, S. M., McNulty, I., Eyberger, C., & Lai, B. (2011). The MicroAnalysis Toolkit: X-ray Fluorescence Image Processing Software [Software]. *AIP Conference Proceedings*, *1365*(1), 196–199. doi: 10.1063/1.3625338

Wilson, C. B. (1961). The Upper Middle Hecla Hoek Rocks of Ny Friesland, Spitsbergen. *Geological Magazine*, *98*(2), 89–116. doi: 10.1017/s0016756800060325

Wörndle, S., Crockford, P. W., Kunzmann, M., Bui, T. H., & Halverson, G. P. (2019, 01). Linking the Bitter Springs carbon isotope anomaly and early Neoproterozoic oxygenation through I/[Ca + Mg] ratios. *Chemical Geology*, *524*, 119–135. doi: 10.1016/j.chemgeo.2019.06.015

Yao, W., & Millero, F. J. (1995, 01). The chemistry of the anoxic waters in the Framvaren Fjord, Norway. *Aquatic Geochemistry*, *1*(1), 53–88. doi: 10.1007/bf01025231

Zendah, H., & Khattech, I. (2015). Standard enthalpy, entropy and Gibbs free energy of for-

mation of "B" type carbonate fluorapatites. *The Journal of Chemical Thermodynamics*, *87*, 29–33. doi: 10.1016/j.jct.2015.03.008

Zhang, F., Stockey, R. G., Xiao, S., Shen, S.-z., Dahl, T. W., Wei, G.-Y., ... Planavsky, N. J. (2022). Uranium isotope evidence for extensive shallow water anoxia in the early Tonian oceans. *Earth and Planetary Science Letters*, *583*, 117437. doi: 10.1016/j.epsl.2022.117437

Zhou, Y., Strandmann, P. A. E. P. v., Zhu, M., Ling, H., Manning, C., Li, D., ... Shields, G. A. (2020, 01). Reconstructing Tonian seawater 87Sr/86Sr using calcite microspar. *Geology*, *48*(5), 462–467. Retrieved from `https://www.researchgate.net/profile/Tianchen\_He/publication/339277615\_Reconstructing\_Tonian\_seawater\_87Sr86Sr\_using\_calcite\_microspar/links/5e4a73ee299bf1cdb9314b03/Reconstructing-Tonian-seawater-87Sr-86Sr-using-calcite-microspar.pdf` doi: 10.1130/g46756.1